

**Whitecap coverage dependence on wind and wave statistics as observed during SO GasEx  
and HiWinGS**

Sophia E. Brumer<sup>1</sup>, Christopher J. Zappa<sup>1</sup>, Ian M. Brooks<sup>2</sup>, Hitoshi Tamura<sup>3</sup>, Scott M. Brown<sup>1</sup>,  
Byron W. Blomquist<sup>4,5</sup>, Christopher W. Fairall<sup>4</sup>, and Alejandro Cifuentes-Lorenzen<sup>6</sup>

<sup>1</sup> Ocean and Climate Physics Division, Lamont-Doherty Earth Observatory, Columbia  
University, Palisades, NY, USA

<sup>2</sup> School of Earth and Environment, University of Leeds, Leeds, UK

<sup>3</sup> Port and Airport Research Institute, Japan

<sup>4</sup> National Oceanic and Atmospheric Association, Earth Systems Research Laboratory, Boulder,  
CO, USA

<sup>5</sup> Cooperative Institute for Research in Environmental Sciences (CIRES), University of  
Colorado, Boulder, CO, USA

<sup>6</sup>Department of Marine Sciences, University of Connecticut, Groton, Connecticut

Corresponding Author: Sophia E. Brumer, Ocean and Climate Physics Division, Lamont-  
Doherty Earth Observatory, Columbia University, 61 Route 9W, Palisades, NY 10964, USA,  
sbrumer@ldeo.columbia.edu

Submitted: Jan 6, 2017

Revised: June 10, 2017

## Abstract

Concurrent wave field and flux measurements acquired during the Southern Ocean Gas Exchange (SO GasEx) and the High Wind Gas exchange Study (HiWinGS) projects permit evaluation of the dependence of the whitecap coverage ( $W$ ) on wind speed, wave age, wave steepness, mean square slope, and wave-wind and breaking Reynolds numbers.  $W$  was determined from over 600 high frequency visible imagery recordings of 20 minutes each. Wave statistics were computed from in situ and remotely sensed data as well as from a WAVEWATCH-III® hind cast. The first ship-borne estimates of  $W$  under sustained wind speeds ( $U_{10N}$ ) of  $25 \text{ m s}^{-1}$  were obtained during HiWinGS. These measurements suggest that  $W$  levels off at high wind speed, not exceeding 10% when averaged over 20 minutes. Combining wind speed and wave height in the form of the wave-wind Reynolds number resulted in closely agreeing models for both datasets, individually and combined. These are also in good agreement with two previous studies (root mean square error  $\sim 0.8\%$ ). When expressing  $W$  in terms of wave field statistics only or wave age, larger scatter is observed and/or there is little agreement between SO GasEx, HiWinGS, and previously published data. The wind-speed-only parameterizations deduced from the SO GasEx and HiWinGS datasets agree closely and capture more of the observed  $W$  variability than Reynolds number parameterizations. However, these wind-speed-only models do not agree as well with previous studies (root mean square error  $\sim 2\%$ ) than the wind-wave Reynolds numbers.

## 1 Introduction

Whitecaps are the surface signature of air-entraining breaking waves consisting of subsurface bubble clouds and surface foam patches. They have been studied extensively since the late 1960s because of the role of bubbles in the air-sea exchange of gases, and the production of sea spray aerosols. They form under wind speeds as low as  $3 \text{ m s}^{-1}$  (Hanson and Phillips 1999; Monahan and O'Muircheartaigh 1986) and have been estimated to cover, on average, 1-4% of the global oceans (Blanchard 1963, 1983). Their high albedo makes them easily detectable locally with cameras set up on stable platforms (e.g., Callaghan et al. 2008a; Lafon et al. 2007; Lafon et al. 2004; Sugihara et al. 2007) as well as from ships (e.g., Callaghan et al. 2008b; Goddijn-Murphy et al. 2011) or planes (e.g., Bobak et al. 2011; Kleiss and Melville 2010). Typically, single-channel visible sensors are used, but whitecap coverage ( $W$ ) has also been determined from multi-channel visible (Randolph et al. 2016) and infrared (Jessup et al. 1997) imagery. Globally,  $W$  can be inferred from satellite-borne microwave radiometers (e.g., Anguelova and Webster 2006; Salisbury et al. 2013).

Being such a readily observable quantity,  $W$  has been recognized as a promising proxy for quantifying wave breaking dependent processes that have complex impacts on the energy, momentum, heat, and mass transfer at the air-water interface. Large-scale wave breaking is the least understood key element in determining the evolution of wave fields and needs to be properly represented in wave models. It generates turbulent kinetic energy in the upper ocean, drives near surface mixing, and transfers energy from the wave system to surface currents and longer waves (Cavaleri et al. 2007). Breaking waves and their consequent whitecaps play a significant role in the climate system (Cavaleri et al. 2012). They directly influence the ocean

surface albedo, and hence the surface radiation budget. It has been estimated that they contribute to a globally averaged cooling of about  $0.03 \text{ W m}^{-2}$  (Frouin et al. 2001). Because of their impact on albedo, whitecaps must be accounted for in remote sensing applications such as retrieval of surface wind (Gaiser et al. 2004) and ocean color (Gordon and Wang 1994).

Many studies have also shown that, through additional turbulence and bubble mediated transfer, wave breaking leads to enhanced air-sea transfer of gases (Asher and Wanninkhof 1998; Monahan and Spillane 1984; Woolf 1997; Woolf et al. 2007). These experiments led to several whitecap dependent gas transfer parameterizations. Furthermore, bursting of the breaking generated bubbles at the surface injects sea spray aerosols into the atmosphere and the aerosol production flux thought to be directly proportional to the whitecap coverage (de Leeuw et al. 2011 and references therein). These sea salt aerosols play an important role in the earth's radiation budget. They act as effective cloud condensation nuclei influencing the microphysical and radiative properties of clouds. They are also direct scatterers of solar radiation (Andreae and Rosenfeld 2008; Haywood et al. 1999).

$W$  has traditionally been parameterized as a non-linear function, most commonly a power law, of the 10-meter wind speed ( $U_{10}$ ) which is easily and routinely measured and modeled. The first empirical function suggested was a simple two coefficient power law (Monahan 1971):

$$W(U_{10}) = aU_{10}^n. \quad (1)$$

Later, a new functional form was proposed that accounts for a minimum wind speed threshold below which no whitecaps are observed (Asher and Wanninkhof 1998), and forced a cubic dependence on wind speed ( $n = 3$ ):

$$W(U_{10}) = a[U_{10} - b]^n. \quad ( 2 )$$

The cubic wind speed dependence was adopted based on the hypothesis that  $W$  is strongly related to the energy flux from the wind which scales as  $u_*^3$  (Phillips 1985; Wu 1988), where  $u_*$  is the air-side friction velocity. However, a cubic dependence on wind speed is questionable and there is no reason not to allow for a tunable exponent. Indeed, satellite derived  $W$  display a dependence on wind speed closer to quadratic (Salisbury et al. 2013) while most recent non-thresholded power-law fits suggest an exponent greater than 3 (APPENDIX A).

Anguelova and Webster (2006) compiled parameterizations of  $W$  as a function of  $U_{10}$  found in the literature prior to 2005. The "wind-speed-only" parameterizations published since then are tabulated in APPENDIX A and plotted in Figure 1. While the historical parameterizations, summarized in Anguelova and Webster (2006), exhibit several orders of magnitude scatter, recent parameterizations can be seen to agree more closely from one study to the next. Different detection techniques used in the past could explain the majority of the scatter in previous studies. Recent advances in instrumentation, and the adoption of an automated and objective image processing algorithm (Callaghan and White 2009), have resulted in more consistent whitecap detection. It is also important to note that parameterizations are typically used over a wind speed range that goes beyond the range over which any given parameterization was determined which may lead to significant errors. Individual projects sample only a limited set of environmental

conditions and exhibit large scatter. This leads to different trends as determined from best fits and parameterizations that diverge from one study to the next. This divergence is exacerbated at the low and high wind speed tails and extrapolating parameterizations beyond their valid range results in increased apparent scatter. However, at least from recent data, at a given wind speed scatter is comparable from one study to the next and the mean  $W$  do not differ significantly (see de Leeuw et al. 2011, Figure 2).

Remaining scatter suggests that wind speed alone does not account for all the observed  $W$  variability. Indeed, a multitude of factors have been recognized to affect wave breaking and bubble lifetime and thereby influencing whitecap coverage (Melville 1996; Salisbury et al. 2013). These include surfactants (Frew 1997), salinity, sea surface temperature (Spillane et al. 1986), atmospheric stability (Myrhaug and Holmedal 2008; Spillane et al. 1986), wind fetch and duration (Myrhaug and Holmedal 2008), current shear, and long wave interaction (Kraan et al. 1996). The effect of these factors are more often than not studied separately. The typical approach is to group observations into several ranges of similar conditions based on one factor and compute different coefficients to the wind speed power laws for each range. Salisbury et al. (2013) looked at the variability in  $W$  after removing the dominant wind speed dependence and showed that the most important secondary factor is the wave state.

Since the scatter displayed by wind-speed-only parameterizations is thought to be largely due to varying wave conditions, parameterizations have emerged in the recent literature that account for both wind speed and sea state. These are summarized in APPENDIX B and APPENDIX C. Zhao

126 and Toba (2001) suggested that  $W$  is better constrained as a function of wind-sea Reynolds  
 127 numbers than wind speed alone. The breaking-wave Reynolds number was first proposed by  
 128 Toba and Koga (1986) and is defined as:

$$R_B = \frac{u_*^2}{\nu_w \omega_p}, \quad ( 3 )$$

129 where  $\nu_w$  is the viscosity of water and  $\omega_p$  is the peak angular frequency of wind waves. Zhao  
 130 and Toba (2001) introduced an alternative Reynolds number:

$$R_{Ha} = u_* H_s / \nu_a, \quad ( 4 )$$

131 where  $H_s$  the significant wave height and  $\nu_a$  is the viscosity of air. Both Zhao and Toba (2001)  
 132 and Woolf (2005) suggested that it is more appropriate to use the viscosity of water rather than  
 133 that of air to characterize wave breaking in the open ocean and suggested:

$$R_{Hw} = u_* H_s / \nu_w. \quad ( 5 )$$

134 Although, these Reynolds numbers were originally defined for wind-seas, subsequent studies  
 135 computed them with wave statistics from the full spectrum which may contain both swells and  
 136 wind-sea (Norris et al. 2013, Goddijn-Murphy et al. 2011). While  $R_{Hw}$  was termed the wave  
 137 roughness Reynolds number in Norris et al. (2013), it will hereafter be referred to as the wave-  
 138 wind Reynolds number to highlight that it incorporates both a wind and wave dependence. Note  
 139 that the Reynolds numbers may also be able to account for the dependence on temperature and  
 140 salinity as these dictate the viscosity (Nayar et al. 2016; Sharqawy et al. 2010).

141

142 The whitecap coverage has also been shown to depend on wave age ( $c_p/u_*$ , where  $c_p$  is the peak  
 143 phase speed), with decreased  $W$  observed in old, swell-dominated seas compared to young, wind-

wave seas (e.g. Schwendeman and Thomson 2015b). For transitional and shallow water waves,  
 an inverse dependence of whitecap coverage on wave age has been observed (Sugihara et al.  
 2007). Based on the relation of  $W$  to the wave-breaking induced energy dissipation as proposed  
 by Komen et al. (1994), Kraan et al. (1996) deduced a relation between  $W$  and the integral wave  
 steepness ( $\bar{\alpha} = \bar{\omega}^4 g^{-2} \int E(\omega) d\omega$ , where  $\bar{\omega}$  is the mean angular frequency and  $E$  is the  
 omnidirectional wave spectrum) :  $W = 24\bar{\alpha}^2$ . Expressing  $\bar{\alpha}$  as a function of wave age, they  
 deduced a wave age dependent parameterization of  $W$ . Multiple later studies (Callaghan et al.  
 2008b; Guan et al. 2007; Lafon et al. 2007; Lafon et al. 2004; Schwendeman and Thomson  
 2015b) have determined additional power law parameterizations of whitecap coverage as a  
 function of wave age. These are tabulated in APPENDIX C. Note that Schwendeman and  
 Thomson (2015b) gave coefficients for the inverse wave age and the parameterization reported  
 in APPENDIX C were computed by fitting a power law to their parameterization.

Fewer studies suggested parameterizations of  $W$  as a function of the turbulent kinetic energy  
 dissipation ( $\varepsilon$ ). This is because only a couple of studies have been undertaken in which both of  
 the near surface  $\varepsilon$  and whitecap coverage were measured (Schwendeman and Thomson 2015b).  
 Such parameterizations will not be addressed in this paper.

The idea that wave breaking occurs once a critical local steepness is reached dates back over a  
 century (Stokes 1880) and is at the core of many probability models of wind-wave breaking.  
 However, few studies have related  $W$  to steepness since Kraan et al. (1996). While local



165 steepness is difficult to measure, average wave steepness parameters are easy to compute from  
 166 1D wave spectra based on a characteristic wave height ( $H$ ) and wave number ( $k$ ):

$$s = \frac{Hk}{2}. \quad (6)$$

167 Typically, either the peak or mean wavenumbers are considered, and the peak, mean or  
 168 significant wave heights are used to compute  $S$  (Kleiss and Melville, 2010; Schwendeman and  
 169 Thomson, 2015b). However, whitecaps are typically associated with steeper and shorter waves  
 170 than the dominant or mean wave system which often corresponds to swell. It has therefore been  
 171 argued that a measure of the mean square slope ( $mss$ ) as suggested by Banner et al. (2002) is a  
 172 more appropriate measure. The  $mss$  is calculated as:

$$mss = \int \frac{(2\pi f)^4 E(f)}{g^2} df, \quad (7)$$

173 where  $E(f)$  is the omnidirectional wave spectral energy density. The frequency range over which  
 174 the  $mss$  is evaluated is typically chosen as the equilibrium range spanning  $\sqrt{2}f_m \leq f \leq \sqrt{5}f_m$   
 175 (Schwendeman and Thomson 2015b), where  $f_m$  is the mean frequency computed as:

$$f_m = \frac{\int f E(f) df}{\int E(f) df} \quad (8)$$

176 Schwendeman and Thomson (2015b) found the  $mss$  most promising for improving  $W$   
 177 parameterization, especially when normalized by directional spread ( $\Delta\theta$ , (Kuik et al. 1988)) and  
 178 frequency bandwidth ( $\Delta f$ ).

179

180 Few parameterizations other than the wind-speed-only have been rigorously tested beyond the  
 181 original studies and not many datasets exist with concurrent  $W$  and wave field measurements.  
 182 The synergy of measurements taken during the Southern Ocean Gas Exchange Experiment (SO

GasEx) and the recent High Wind Gas exchange Study (HiWinGS) offer unique datasets that facilitate testing of new and existing  $W$  parameterizations. In this paper, the dependence of whitecap coverage on wind speed and sea state conditions is investigated with the aim of improving whitecap parameterizations to be used in gas transfer and climate models. The SO GasEx and HiWinGS field campaigns are described in Section 2 along with details of supporting measurements and of the WAVEWATCH III® hind cast used to complement in situ wave observations. After a brief explanation of the image processing and wave field analysis methods in Section 3, the results are presented in Section 4 and discussed in Section 5. Section 6 summarizes key findings and provides recommendations for whitecap parameterizations and future studies.

## 2 Data

### 2.1 The SO GasEx cruise

The SO GasEx cruise was the third and most recent cruise of the US led GasEx series initiated in 1998. The main GasEx objective was to improve quantification of air-sea CO<sub>2</sub> fluxes and gas transfer velocities. The aim of this third cruise was to examine these processes at higher wind speeds and obtain data in a previously unexplored region. The SO GasEx project focused on a study area around 51°S, 36°W, where the *R/V Ronald H. Brown* remained for 37 days having left Punta Arenas, Chile, on 28 February 2008 (Figure 2a). It is important to note that the ship was rarely stationary as deliberate tracer release surveys were conducted on site. The study location was chosen for its high wind speeds and large air-water pCO<sub>2</sub> difference. The average  $U_{10N}$  measured in the main study location was  $9.7 \pm 3.2 \text{ m s}^{-1}$ , and a maximum wind speed of  $20.7 \text{ m s}^{-1}$

was recorded during transit back to Uruguay where the cruise ended on 9 April 2008 (Figure 3a). In order to avoid a storm between 13 and 17 March, the *R/V Ronald H. Brown* moved temporarily into the lee of South Georgia Island. Water temperatures in the study site varied between 5°C and 7°C, increasing to 14°C in the transit legs. For further details about SO GasEx, see Ho et al. (2011), Edson et al. (2011) and Cifuentes-Lorenzen et al. (2013).

## 2.2 The HiWinGS cruise

With the aim of gaining new insights into poorly understood aspects of air-sea interaction under high winds, the HiWinGS cruise objective was to deploy direct measurements of trace gas and physical fluxes together with a suite of wave physics and sea state observations. The HiWinGS cruise took place on board the *R/V Knorr*, in the North Atlantic, (Figure 2b) departing Nuuk, Greenland, on 9 October 2013 and ending at Woods Hole, USA on 14 November 2013. The ship's track was chosen based on daily analysis of weather maps and forecasts from the European Centre for Medium-Range Weather Forecast model provided by the Icelandic Met Office as well as from PassageWeather.com with the aim of maximizing the amount of time spent in the strongest winds. Along the track, the ship stopped at several stations for buoy deployments. While on station, the ship was positioned bow pointing into the wind for the duration of each storm.

The ship remained in the Labrador Sea, south of Greenland, for the first ~20 days of the cruise. Sea surface temperature and salinity were around 6-8°C and 34-34.5 psu, respectively, at the first 6 stations (Figure 2b). The ship then transitioned through the Gulf of St Lawrence from 4 to 6

November 2013, and the last station was south of Nova Scotia where warmer and higher salinity Gulf Stream waters were encountered with SST of 20°C and salinity of 36 psu. Wind speeds exceeded 15 m s<sup>-1</sup> 25% of the time amounting to a total of 189 hours of wind speeds above 15 m s<sup>-1</sup> of which 48 hours had wind speeds greater than 20 m s<sup>-1</sup>. On 25 October 2013 (station 4), wind speeds exceeded 25 m s<sup>-1</sup> with gusts of 35 m s<sup>-1</sup> in the early stages of what became known as the St. Jude's day storm (Figure 3b).

### 2.3 Visible Imagery

During SO GasEx a total of 216 20-minute video segments were recorded, while during the HiWinGS cruise over 500 20-minute segments were recorded, of which 50 were taken during the St. Jude's day storm. For both experiments, the imaging system consisted of two obliquely-angled Imperx model Lynx 1M48 digital video cameras with a sensing array of 1000 x 1000 elements of 7.4 µm. These were mounted on the flying bridge of the *R/V Knorr* and *R/V Brown* at a height above the water line of 14.7 m and 25 m, respectively. For both experiments, one of the cameras was directed starboard while the other one was mounted on the port side to accommodate all lighting conditions. During HiWinGS, wide field-of-view lenses (68.7° FOV; 6 mm focal length) were used, whereas during SO GasEx lenses with 9 mm focal length and a FOV of 36.6° were used. The visible cameras ran at a frame rate of 20 Hz during HiWinGS and 5 Hz during SO GasEx.

The imaging system was improved for HiWinGS by the addition of Inertial Motion Units (IMU) mounted on the same metal plate as the cameras to record the pitch, roll and yaw angles of the

cameras. An Xsens model MTi IMU was mounted on the port side system while a 3DM-GX2 model MicroStrain IMU was affixed to the starboard camera mount. The Xsens, which has an angular resolution of 0.05°, recorded at ~100 Hz, while the MicroStrain, which has an angular resolution of <0.1°, recorded at 50 Hz. Both sensors have a dynamic accuracy of  $\pm 2.0^\circ$ .

#### *2.4 Meteorological Measurements*

Momentum, energy, and buoyancy fluxes were obtained via direct eddy covariance measurements during both SO GasEx and HiWinGS, along with mean measurements of wind speed, wind direction, air temperature, humidity, pressure, and downwelling solar and IR radiation. The University of Connecticut Direct Covariance Flux System (Uconn DCFS; Edson et al. 1998; Edson et al. 2004) and the NOAA/ESRL/PSD system (Blomquist et al. 2006; Fairall et al. 2003) were deployed during SO GasEx. These were mounted on the jackstaff of the *R/V Brown* at a height of 18 m above the surface and consisted of 3 fast response Gill R-3 sonic anemometers, and 5 infrared gas analyzers (Li-Cor LI-7500) sampling at 20 Hz. Additionally, the systems included a GPS compass and Systron-Donner "Motion-Pak" used to correct for ship motion as described by Edson et al. (1998). For a detailed description of the setup, the reader is referred to Edson et al. (2011).

The NOAA/ESRL/PSD wind-motion system was also used during HiWinGS. It was mounted on the bow mast at 16 m above the water line with fast response sensors set to sample at 10 Hz. Two additional sonic anemometers were deployed, a Gill model R2 from the University of Hawaii (UH) on the foremast at 15 m and a Gill Windmaster Pro from Plymouth Marine

Laboratory on the main mast, some distance behind the bow. While the measurements are mostly consistent between systems, only the measurements from the UH sonic and the Motion-Pak are considered here as the NOAA system suffered a power outage during the St. Jude storm that put several instruments out of action. Direct eddy covariance fluxes and bulk fluxes from the COARE3.5 algorithm (Edson et al. 2013; Fairall et al. 2003; Fairall et al. 2011) were computed over 15 minute intervals for SO GasEx and hourly for HiWinGS.

## 2.5 1D and Directional Wave Spectra

### 2.5.1 *In situ and remotely sensed measurements*

Directional ocean wave spectra were obtained with a Wave and Surface Current Monitoring System (WaMoS® II) during SO GasEx (Cifuentes-Lorenzen et al. 2013; Lund et al. 2016). These measurements are based on the radar backscatter of sea clutter in which the wave patterns are distinguishable. The system used the unfiltered output from a marine X-Band radar mounted on the flying bridge of the *R/V Brown* operating at 9.41 GHz to determine wave and surface current parameters. The WaMoS® II has the capability to resolve two-dimensional maps of the surface elevation, and allowed for continuous day and night real-time measurements even in rough seas and harsh weather conditions. WaMoS® II provides directional wave spectra and individual wave state components at scales of  $O(100\text{ m})$ .

During HiWinGS, a Datawell DWR-4G Waverider buoy of 0.4 m diameter was deployed while on station for the duration of each major storm system. The Waverider uses the Doppler shift of the GPS signal carrier wave to obtain a direct measurement of its velocity in 3 dimensions at

1.28 Hz. These are integrated to obtain a time series of the 3-dimensional displacement, from which directional wave spectra can be derived. The spectral frequency range resolved by the Waverider covers 0.025 Hz to 0.6 Hz, corresponding to waves of wavelength greater than 4.3 m. During most deployments, the Waverider was left to drift freely within 5 km of the ship. The Waverider was tethered to the ship with a 200 m polypropylene line during the first deployment due to operational restrictions and during the largest storm (station 4) due to severe wind and wave conditions that would not have allowed the ship to stay within radio contact of the buoy. While the tether remained slack and the buoy was kept outside of the ships wake on the first deployment, it regularly dragged the buoy under water during the peak wind period on station 4. This led to loss of GPS reception and poor data quality during part of the St. Jude storm. These data were disregarded for subsequent analysis.

In addition, short to moderate gravity waves were measured using a Riegl laser altimeter (model LD90-3100VHS) during both experiments. The laser operates at a wavelength of 0.9  $\mu\text{m}$  (near infrared), with a beam divergence of 2.7 mrad that corresponds to a footprint on the ocean surface of 2.65 cm at a range of 10 m. The manufacturer-specified measurement accuracy is  $O(2.0\text{ cm})$  with a precision of  $O(0.25\text{ cm})$ . The LD-90 laser altimeter data independently characterized spatial and temporal properties of the wave height field resolved down to  $O(20\text{ cm})$  wavelengths (Zappa et al. 2012).

The Reigl was mounted on the jackstaff of the *R/V Knorr* at about 14.4 m during HiWinGS and on the jackstaff of the *R/V Brown* at 10 m above the mean water level during SO GasEx. Internal

processing provided range to surface measurements at 10 Hz which were corrected for the ship's heave following Cifuentes-Lorenzen et al. (2013) to provide the wave surface displacement. Midway through HiWinGS, after the St. Jude storm on 25 October 2013 at station 4 (see Figure 2), the Riegl stopped functioning due to a power distribution failure.

#### 2.5.2 WAVEWATCH-III® hind cast

As flux measurements were taken continuously during the HiWinGS cruise and visible imagery was taken regularly during daylight periods regardless whether the ship was steaming or on station, the in situ wave data were complemented by a model hind cast. Version 3.14 of the Wavewatch-III<sup>TM</sup> (WW3; Tolman 2009) was used to compute the hind cast for the duration of the cruise from 1 October to 15 November 2013 (2.5 months). The model domain was set to cover the North Atlantic (0°-70°N and 100°W-15°E) with a latitudinal and longitudinal grid resolution of 0.2°. Bottom topography and coastlines were taken from the ETOPO2 dataset that provides 2 minute gridded elevations/bathymetry for the world. The wave model was forced by 6-hourly surface wind fields from the National Centers for Environmental Prediction/Climate Forecast System Reanalysis (NCEP/CFSR) product (Saha et al. 2010) which has a horizontal resolution of ~38 km (Gaussian Grid: T382).

WW3 solves the wave spectral balance equation which dictates the evolution of the wave field based on the sum of source terms consisting of the energy transferred to the waves by the wind ( $S_{in}$ ), the energy lost through dissipation due to wave breaking ( $S_{dis}$ ), and nonlinear wave-wave energy transfers ( $S_{nl}$ ):



$$\frac{DN}{Dt} = \frac{S_{\Sigma}}{\sigma} = (S_{in} + S_{nl} + S_{dis})/\sigma, \quad (9)$$

337 where  $N = N(t, x, y, f, \theta)$  is the wave action density spectrum,  $S_{\Sigma}$  the sum of source terms, and  
 338  $\sigma$  the intrinsic (radian) frequency. The term  $\frac{DN}{Dt}$  denotes the total time derivative:  $\frac{DN}{Dt} = \frac{\partial N}{\partial t} +$   
 339  $\nabla_x((\mathbf{c}_x + \mathbf{u})N) + \nabla_i(\mathbf{c}_i N)$ , where  $\mathbf{u}$  is the current,  $\mathbf{c}_x$  the propagation, i.e. group velocities in  
 340 geographical space  $(x, y)$  and  $\mathbf{c}_i$  the propagation velocities in spectral space  $(f, \theta)$ .

341

342 For the HiWinGS hind cast, the source terms proposed by Tolman and Chalikov (1996) were  
 343 used and the surface wind speed at 10 m elevation was modified to account for the instability of  
 344 the atmospheric boundary layer (the “effective” wind speed; Tolman et al. 2002). Being a third-  
 345 generation model, WW3 allows for a punctual, although approximate, representation of  $S_{nl}$  for  
 346 which the discrete interaction approximation (DIA) method was chosen (Hasselmann et al.  
 347 1985). For spatial propagation of the wave spectrum, the default third-order advection scheme  
 348 was used.

349

350 The spectral space was discretized using 35 frequencies ranging from 0.04 Hz to 1.05 Hz in  
 351 10% steps ( $f_{i+1} = 1.1f_i$ , where  $i$  is a discrete grid counter) with 36 directions ( $\Delta\theta = 10^\circ$ ). An  $f^{-5}$   
 352 spectral tail outside the model frequency range was assumed, as per default WW3 settings. The  
 353 directional wave spectra from the hind cast were stored every 30 minutes along 4 trajectories  
 354 following the ship’s track.

355

## 3 Methods

### 3.1 Image Analysis

Initial visual quality control led to removal of runs that were affected by sun glare, or taken in otherwise poor light conditions. Runs were also removed based on the presence of birds that tend to be falsely identified as whitecaps. The first step of the image analysis was to crop the images in order to avoid the ship's wake when the ship was steaming and to remove the horizon from the field of view. An example of images taken while on station during HiWinGS is shown in Figure 4a. Next, whitecap pixels were identified for every individual cropped raw image. Before applying the typical brightness threshold (Callaghan and White 2009) to the images, all background gradients were removed. This was achieved in a two-step process: the images are pre-thresholded to identify any pixel with brightness greater than 3.25 standard deviations above the mean, then the row and column means are computed ignoring the high brightness pixels and subtracted from each pixel. Pre-thresholding avoids brightness bleeding when removing background gradients.

Removing background gradients was found to greatly improve subsequent whitecap detection via the typical automated brightness threshold techniques. A test dataset was used to evaluate the effectiveness of flattening the background intensity gradient for removing biases arising from varying brightness and exposure settings. This dataset consisted of imagery taken over the course of two days during HiWinGS from two Mobotix MX-M24M IP cameras with 32 mm lenses, providing a 60° field of view, on the starboard side of the *R/V Knorr* with closely matched fields of view. One camera setting remained unchanged during the test while the target brightness and

exposure settings were changed on the other one. Ignoring the background gradients resulted in up to a factor 4 difference between  $W$  determined from the two cameras, removing them reduced the difference to a factor of 0.7 to 1.04.

Whitecaps were then isolated in the pre-processed rectified images by the automated whitecap extraction (AWE) algorithm (Callaghan and White 2009) which computes the most suitable brightness threshold for each individual image based on the derivatives of an image structure function. The AWE algorithm has been used successfully to analyze large datasets (Callaghan et al. 2008a; Callaghan et al. 2008b; Goddijn-Murphy et al. 2011; Scanlon and Ward 2013, 2016; Schwendeman and Thomson 2015b; Schwendeman et al. 2014) and has been shown to provide robust  $W$  results.

The thresholded images are orthorectified to compute  $W$ . This is achieved by first correcting for lens distortion based on intrinsic parameters determined using the Camera Calibration Toolbox for Matlab<sup>®</sup> (Bouguet 2015). The effect of the lens distortion can clearly be seen in the non-cropped raw imagery in Figure 4a and its correction in Figure 4b). Then, geo-rectification is performed by applying the 3D rotation matrix based on the roll, pitch, and yaw angles (Holland et al. 1997; Schwendeman and Thomson 2015a). This step is illustrated on the raw imagery in Figure 4c and Figure 4d. Finally the thresholded images are interpolated onto the regular georectified grid with pixel dimensions of  $0.01\text{m}^2$  (Figure 4e),  $W$  is determined for each image and an average  $W$  is computed for each 20-minute segment.

At this point, an additional quality control step was undertaken and a cumulative whitecap coverage  $W_{CA}$  was computed based on the whitecap coverage ( $W_{frame}$ ) determined from a single frame ( $F$ ), normalized by the 20-minute averaged whitecap coverage ( $W_{20min}$ ):

$$W_{CA_{norm}}(F) = \frac{W_{CA}(F)}{W_{20min}} = \left( \sum_{i=1}^F \frac{W_{frame}(i)}{F} \right) / W_{20min}$$

Time series of  $W_{CA_{norm}}$  show that for the most part  $W_{CA_{norm}}$  converges quickly towards unity staying within 1 standard deviation bounds  $\pm 0.3$  and  $\pm 0.17$  after 10 and 15 minutes, respectively (Figure 5). Several runs, however, do not appear to converge within 20 minutes. Non-converging  $W_{CA_{norm}}$  were identified based on standard deviation bounds computed from  $W_{CA_{norm}}$  of the entire dataset for a given time (or frame number). Data was flagged if it fell outside the 2 standard deviation bound after 15 minutes and excluded from subsequent analysis. There does not seem to be a clear dependence of the convergence time on wind speed or wave age which could require a wind and sea state dependent averaging timescale. Note that an alternative approach to evaluate convergence of  $W$  can be found in Callaghan et al. (2008a).

After removing these data, the 20-minute  $W$  estimates were averaged to give hourly estimates on the same time intervals as the fluxes yielding 97 and 176 hourly means for SO GasEx and HiWinGS, respectively. Note that when comparing  $W$  to wave statistics, the number of hourly concurrent data points is 73 for SO GasEX and 172 for HiWinGS which is further reduced to 34 and 138 when considering wind seas for SO GasEx and HiWinGS, respectively.

While an IMU was mounted in each camera housing during the HiWinGS campaign recording the rotation angles that allow for projection and scaling of the images, this was not the case during SO GasEx. Instead, rotation angles were determined by tracking the horizon (Schwendeman and Thomson 2015a). In order to test the performance of the horizon tracking algorithm, it was applied to the HiWinGS imagery and the computed angles were plotted against those computed from the IMUs. As shown in Figure 6, the horizon tracking algorithm is successful at retrieving the roll and pitch angles. However, it generates erroneous attitude angles easily detectable as spikes in the pitch and roll time series. Depending on the type of analysis to be subsequently performed on the imagery, individual frames may be discarded or de-spiking algorithms (e.g. Mori et al. 2007) may be applied.

### *3.2 Wave-field Statistics*

Wave field statistics were determined both from the directional spectra given by the Waverider, the WAMOS, and the WW3 hind cast and the 1D spectra obtained from the Riegl. The raw 3D displacement measurements of the Waverider were used to compute hourly spectra using the DIWASP toolbox (Johnson 2012) to match the time scale of the other data. Half hourly wave spectra obtained from the four WW3 hind cast tracks were averaged to get hourly spectra. Figure 7 shows the spectrogram and an example of a directional spectrum from the WAMOS, those from the Waverider and WW3 are shown in Figure 8.

Wave statistics were first computed from 1D spectra measured by the Riegl or from the directionally integrated spectra of the WAMOS, Waverider and WW3 using a standard

processing method. Similarly, a standard protocol was applied to the directional spectra to separate wind seas and swell and to get wave statistics for individual wave groups (Hanson and Phillips 2001). The computed wave statistics include the peak ( $f_p$ ) and mean ( $f_m$ ) frequencies, the peak and mean phase velocities ( $c_p$  and  $c_m$ , respectively) as well as the significant ( $H_s = 4[\int E(f)df]^{1/2}$ ), peak ( $H_p = 4[\int_{0.7f_p}^{1.3f_p} E(f)df]^{1/2}$ ) and mean ( $H_m = 4[\int_{0.7f_m}^{1.3f_m} E(f)df]^{1/2}$ ) wave height of the entire wave field or individual wave system. When computing statistics for individual systems, we distinguish between wind-sea and swells, merging systems so as to have at the most a single wind sea and a single swell system.

No comparison of the statistics obtained from the different datasets is discussed here. Inter-comparison of various wave measurements and validation of the WW3 hind cast for HiWinGS will be reported in a separate paper along with a detailed description of the analysis methods applied to the directional spectra. An inter-comparison between the Riegl and WAMOS data recorded during SO GasEx can be found in Cifuentes-Lorenzen et al. (2013), while Lund et al. (2016) show a comparison of wind-sea and swell statistics obtained from WAMOS and WW3 for SO GasEx. As the statistics obtained from the various datasets are consistent for each experiment, results are reported based on WAMOS and WW3 statistics to allow usage of the full range of whitecap data.

### 3.3 Determination and evaluation of parameterizations

Wind and wave dependent parameterizations are determined through weighted least square fits of binned data for each dataset individually and combined. The binning was done using the

equi-density method with each bin containing 7 data points, rather than at regular intervals of wind and/or wave statistics. . The reciprocal of the standard error in each bin was used as weights. Two fit statistics are reported to help evaluate how the parameterizations: 1) The root mean square error ( $rmse = \sqrt{\sum (W_{obs} - W_{param})^2 / N}$ , where  $W_{obs}$  are the hourly estimates of  $W$ ,  $W_{param}$  are the  $W$  obtained from the parameterizations and  $N$  the number of estimates), and 2) The correlation coefficients ( $r^2 = 1 - \frac{\sum (\log_{10} W_{obs} - \log_{10} W_{param})^2}{\sum (\log_{10} W_{obs} - \overline{\log_{10} W_{obs}})^2}$ , where the overbar represents the dataset average) computed as in Schwendeman and Thomson (2015b) based on the log-residual so as to equally weight data points across orders of magnitude. Note that all fits were performed in linear space and both  $W$  and the  $rmse$  are reported in %. Note also that no consistent way of computing the  $rmse$  has been used in the literature and that these therefore are not directly comparable to previous studies such as Schwendeman and Thomson (2015b) and (Goddijn-Murphy et al. 2011).

## 4 Results

### 4.1 Whitecap dependence on wind speed alone

Following the traditional approach, the dependence of  $W$  on wind speed alone is assessed. As seen in Figure 9a, the So GasEx and HiwinGS data fall right on top of the recent wind speed only parameterizations reported in the literature since 2004.

Results of the weighted least-square fit for a thresholded power law (EQ. 2) are listed in Table 1 along with the appropriate fit statistics. The power law fits to the individual and combined datasets agree closely with exponents closer to 1 than 3. It appears that the whitecap coverage

saturates at high wind speeds ( $U_{10N} > 22.5 \text{ m s}^{-1}$ ). The fit to the combined dataset most closely follows that suggested by Salisbury et al. (2013) based on the 10 GHz microwave satellite data. The *rmse* between the best fits determined here and the 10 GHz parameterization of Salisbury et al. (2013) is around 0.1%. The next closest parameterization is that of Goddijn-Murphy et al. (2011, Eq. A, Appendix A) with an *rmse* to the best fit to the combined data set of 1.4%. The *rmse* between the best fits determined here and the other parameterizations plotted in Figure 9a average around 2%.

Following the same approach as before, parameterizations of  $W$  as functions of the friction velocity were determined from the data. These are shown in Figure 9b and listed in Table 1. Parameterizations from previous studies plotted here are summarized in Appendix D. Based on the fit statistics, there does not seem to be an improvement in using the friction velocity over the 10-m neutral wind speed. Again, the exponents of the thresholded power laws suggest a more close to linear than cubic relationship between  $W$  and  $u_*$ .

#### 4.2 Whitecap dependence on sea state alone

In terms of pure sea state parameterization, the relationship between  $W$  and various forms of wave steepness parameters ( $S$ ) and ( $mss$ ) were investigated. These statistics were computed from entire spectra as well as from the wind-sea-only partition. To compute  $S$ , three distinct wave heights ( $H_s$ ,  $H_m$ , and  $H_p$ ) were considered in combination with the two wave numbers ( $k_p$  and  $k_m$ ) computed via the linear deep water dispersion relation ( $k = (2\pi f)^2/g$ ) from the peak and the mean frequency, respectively.



507

508 Simple power laws of the form  $W(X) = aX^n$  were found to be more suitable than thresholded  
509 power laws for these statistics. The computed fits are listed in Table 2 along with the appropriate  
510 statistics. Based on the correlation coefficients ( $r^2$ ), steepness and slope parameters are poorer  
511 predictors for  $W$  than wind speed. Negative  $r^2$  suggest that the model performs worse than a  
512 horizontal line. The root mean square errors ( $rmse$ ) are also generally higher than for the wind  
513 only fits. In general, very poor fits were obtained for SO GasEx. Of the wave steepness  
514 predictors,  $\frac{H_s k_m}{2}$  gives the best fit for HiWinGS. Normalizing the  $mss$  by the directional spread  
515 and the frequency bandwidth yields only slightly improved fits. These two fits are shown in  
516 Figure 10. They correspond to the steepness estimate and the normalized  $mss$  that were shown to  
517 best fit the Northeast (NE) Pacific data published by Schwendeman and Thomson (2015b).  
518 While the HiWinGS data appear to fall along the best fit suggested by Schwendeman and  
519 Thomson (2015b) when plotted against the wave steepness  $\frac{H_s k_m}{2}$ , significantly higher  $W$  were  
520 observed over less steep waves during SO GasEx than by Schwendeman and Thomson in the NE  
521 Pacific. More importantly, the SO GasEx data show very little variation of  $W$  with wave  
522 steepness, regardless of the wave statistics used. Neither dataset shows much variation with  $mss$   
523 whether normalized or not. Considering only the wind-sea part of the spectrum does not improve  
524 the fits or increase the sensitivity of  $W$  to the slope estimates.

525

#### 526 4.3 Combined influence of wind and wave field on Whitecap coverage

527 The first metric considered that includes the combined effect of wind and wave field is the wave  
528 age. The wave age has been derived both in terms of  $u_*$  and  $U_{10N}$  as well as from the mean and

peak phase speeds ( $c_m$  and  $c_p$ ) of both the wind-sea and total spectra. As for the wave slope parameters, a non-thresholded power law fit was computed for the various wave age estimates (see Table 3). Shown in Figure 11 are the whitecap coverage plotted against the wave age expressed both in terms of  $U_{10N}$  and  $u_*$  and the peak velocity of the total and wind-sea wave field. While overall better fits were found when the wave age was expressed as a function of  $c_m$ , as was the case in Schwendeman and Thomson (2015b), plots of the wave-age as a function of  $c_p$  are shown here to illustrate how the SO GasEx and HiWinGS data compare to previous studies that addressed the wave-age dependence of  $W$ .

Both datasets in Figure 11a agree once more with that of Schwendeman and Thomson (2015b), and  $W$  is higher than reported in all other studies for a given wave age. Interestingly, when considering wind seas alone (Figure 11b and 11d), the two datasets presented here no longer show matching trends, and the SO GasEx  $W$  is lower than the HiWinGS  $W$  for a given wave age. The  $W$  magnitude for a given wave age during HiWinGS is similar for the total and the wind-sea derived wave age because the wind-sea partition often contained the dominant peak. Since swell was typically dominant during SO GasEx, the change in  $W$  magnitude between total wave age and wind-sea wave age suggests less breaking occurs when a young wind sea was superimposed on swell than in an overall young sea.

The wave-wind and breaking-wave Reynolds numbers are the second type of non-dimensional parameters historically used to parameterize  $W$  including both wind and sea state dependence. When computing the wave-wind Reynold numbers ( $R_H$ ), the significant ( $H_s$ ), mean ( $H_m$ ), and

peak ( $H_p$ ) wave heights were considered. Similarly, when computing the breaking-wave Reynolds number ( $R_B$ ), the peak ( $\omega_p$ ) and mean ( $\omega_m$ ) angular velocities were considered. Again, both the full spectrum and the wind-sea only statistics were considered and least square fits were used to determine non-thresholded power laws relating  $W$  to the Reynolds numbers. The viscosities were computed based on the ships underway temperature and salinity measurements using the MATLAB Seawater Thermophysical Properties Library (Nayar et al. 2016; Sharqawy et al. 2010). Results are summarized in Table 4 and Table 5. Two examples are shown in Figure 12. Overall, the wave-wind Reynolds number fits show very good agreement between the datasets as well as with the findings of Goddijn-Murphy et al. (2011) and Scanlon and Ward (2016). The *rmse* between the fits determined here and for Goddijn-Murphy et al. (2011; Eqs. D and E in Appendix B), and for Scanlon and Ward (2016; Eq. B in Appendix B) all average around 0.8%. Note that the parameterization of Zhao and Toba (2001) had to be adapted for this plot as they compute the wave-wind Reynolds number using the air viscosity rather than the water viscosity. A nominal  $v_a$  to  $v_w$  ratio of 11.03 was chosen. For the breaking-wave Reynolds number, there is poorer agreement between datasets as well as with prior studies, though scatter appears to be reduced. Note again that previous parameterizations were adapted as the breaking Reynolds number has typically been reported in terms of the air rather than the water viscosity.

#### 4.4 Multiple parameter model

As alluded to in section 4.3, the dependence of  $W$  on wind and wave field parameters can be studied through dimensionless parameters. It is apparent that  $W$  may depend on  $(c, \rho_a, \rho_w, u_*, g, H, k, \Gamma, X)$ , where  $\rho_a$  and  $\rho_w$  are the densities of air and water, respectively,  $u_*$  is

573 the friction velocity in air,  $g$  the acceleration due to gravity,  $H$  a characteristic wave height,  $k$  a  
 574 characteristic wavenumber,  $\Gamma$  the surface tension coefficient and  $X$  the wave fetch.  
 575 Considering non-dimensional scaling, the whitecap coverage can be written as

$$W = f\left(\frac{\rho_a}{\rho_w}, \frac{c}{u}, S, Re, F, B_o\right). \quad (10)$$

576 Here,  $\frac{c}{u}$  is the wave age,  $S$  is a measure of the wave steepness,  $Re$  the wave-wind or breaking-  
 577 wave Reynolds number (see equations ( 3 ), ( 4 ) and ( 5 )),  $F$  the dimensionless fetch ( $F = \frac{gX}{c_p^2}$  or  
 578  $F = \frac{gX}{u_*^2}$ ), and  $B_o$  the Bond number ( $B_o = \Delta\rho g\Gamma^{-1}$ ). The dimensionless group  $\frac{\rho_a}{\rho_w}$  is approximately  
 579 constant and can be ignored. As waves small enough to be directly affected by surface tension  
 580 ( $\Gamma$ ) are not resolved in the measurements, the Bond number dependence is ignored. Furthermore,  
 581 not having a measure of fetch, waves will be assumed to be fetch unlimited. This leads to a  
 582 simplified model

$$W = f\left(\frac{c}{u}, S, Re\right), \quad (11)$$

583 Assuming a power law dependence of  $W$  on the non-dimensional numbers, we can rewrite ( 11 )  
 584 as follows:

$$W = aX, \quad (12)$$

$$\text{Where } X = \left(\frac{c}{u}\right)^\alpha S^\beta Re^\gamma$$

585 The coefficients  $\alpha$ ,  $\beta$ , and  $\gamma$  can be found by minimizing a squared-difference cost function. This  
 586 is done by taking the log on both sides of ( 12 ) and solving the following linear regression:

$$\log_{10} W = \log_{10} a + \alpha \log_{10} \left(\frac{c}{u}\right) + \beta \log_{10} S + \gamma \log_{10} Re. \quad (13)$$

587

Choosing  $S = \frac{H_m k_m}{2}$ ,  $Re = \frac{u_* H_m}{\nu_w}$ , and a wave age expressed in term of the friction velocity and the mean phase speed computed from the whole wave spectrum, coefficients were computed for each dataset individually and combined. The model determined from the combination of both datasets is shown in Figure 13. The coefficients resulting from the linear regressions are quite different for each dataset and regressions suggest that including the steepness does not significantly improve the model (Table 6). Indeed, T statistics suggest that  $\beta = 0$  at a 91.4%, 24.7% and 77.6% confidence level for HiWinGS, SO GasEx, and the two combined. Fit statistics ( $r^2=0.52$ ;  $rmse \sim 1.39$ ) suggest that multiple parameters capture more of the variability in the observed  $W$  than single parameter wind and wave dependent models. Lack of agreement between the regression results however does not support using a multi non-dimensional parameter model as expressed by Eq. (13). Note that both the wave age and the Reynolds numbers combine wind and wave characteristic, but have opposite impacts on  $W$ . It may therefore be more physically intuitive to combine only one of these two non-dimensional number with the pure sea state parameter that is steepness. However statistically, combining only two non-dimensional numbers rather than 3 led to poorer results. As the Reynolds numbers capture most of the variance of  $W$  of the non-dimensional numbers considered here,  $W(S, Re)$  is a better model than  $W(S, c/u)$ .

## 5 Discussion

Careful considerations need to be made before using parameterizations beyond their range of validity. Extrapolations, while often unavoidable, increase uncertainties and may lead to erroneous results. Ongoing efforts and targeted field campaigns allow for an ever-wider range of

environmental conditions to be sampled, and a combined dataset will lead to more precise and universal parameterizations. New parameterizations should clearly state the range for which they are valid. This was done for the results reported here and as far as possible for the parameterizations compiled from the existing literature.

Prior studies not only differ in the whitecap detection algorithms used, but also in the application of appropriate image projection and scaling. In order to evaluate the impact of image scaling on the whitecap coverage estimate, we compared results from SO GasEx computed with or without scaling. For a given frame, image scaling significantly alters  $W$ , however, when computing 20-minute averaged  $W$  the impact of scaling appears to average out. The scaling has minimal impact when considering over 6000 frames as illustrated in Figure 14. Recording attitude angles and geo-rectifying images is therefore not essential when computing  $W$ , but is critical when tracking breakers such as for determining the breaking crest length distribution.

When considering wind speed only and wave-wind Reynolds number parameterizations, the level of agreement between the two datasets analyzed in this study with existing parameterizations is remarkable. Close agreement between these two datasets and recently published parameterizations gives confidence in the recently-developed and now commonly-used thresholding technique, and it may be valuable to reanalyze old datasets with the same method if possible. The additional step of removing background gradients before running the AWE (Section 3.1), ensures removal of biases arising from varying light conditions and camera exposure and brightness settings. A similar approach was put forward by Mironov and Dulov (2008). Agreement between the WW3 hind cast wave statistics and in-situ observations is also remarkable (Figure 8). This should encourage reanalysis of wave dependent whitecap

parameterizations for earlier datasets using hind casts to complement measurements, to evaluate them over a wider range of conditions.

Recent wind-speed-only total whitecap parameterizations showing less scatter than previously suggested for intermediate to high wind speeds. When considered within their originally defined wind speed range, they fall within 30% of their average, spanning an order of magnitude, for  $U_{10} > 10 \text{ m s}^{-1}$ . Note that the datasets presented here are much larger than those obtained from previous field experiments. Therefore, a larger amount of variability may be expected. Indeed, the data presented here displays variability similar to that of the combined historical datasets (c.f. Albert et al. (2016), Figure 1), which is greater than reported in individual studies. Significant scatter of up to 2 orders of magnitude remains in hourly  $W$  observations at many wind speeds and further studies are necessary to thoroughly understand it. While surfactants have been shown to prolong the lifetime of foam at the water surface (e.g., Garrett, 1967; Callaghan et al. 2016) and their spatial inhomogeneity may account for some of the observed scatter for a given wind speed and sea state, they are difficult to measure under wind speeds greater than  $10 \text{ m s}^{-1}$  (Cunliffe and Wurl, 2014). Technological development and more observations are evidently needed to further the field.

Targeted sampling under high winds and young sea conditions during HiWinGS extended the upper limit of the validity range for wind only whitecap parameterizations to  $25 \text{ m s}^{-1}$ . It is important to note here that unlike the majority of previous studies, the neutral 10-m wind speed

( $U_{10N}$ ) was considered here. Both Goddijn-Murphy et al. (2011) and Salisbury et al. (2013) used equivalent neutral winds and, therefore maybe not surprisingly, match the parameterizations determined in the current study the best. The neutral wind speed and friction velocity along with non-dimensional numbers calculated from them are the only quantities that account for varying atmospheric stability conditions and therefore allow for true comparison from one dataset to the next. The differences in whitecap parameterizations arising from the stability dependence and correction has been evaluated by Paget et al. (2015).

As hinted to by Schwendeman and Thomson (2015b) and Callaghan et al. (2008b),  $W$  is seen to level off at high wind speed (c.f. Figure 1 and Figure 9a), not exceeding 10% when averaged over a 20 minute to hourly period. To evaluate  $W$  saturation at high winds, linear fits were performed through the high wind speed data points and T-tests were used to determine if the slopes were significantly different than zero. T-tests reveal that for  $U_{10N} > 18 \text{ m s}^{-1}$  (26 hourly averages), the slope of  $W$  vs.  $U_{10N}$  is significantly different than zero only at a 14% confidence level, i.e.  $W$  is near constant. If the lower wind speed bound is reduced to  $17.5 \text{ m s}^{-1}$ , the confidence that the slope is significantly different than zero is raised to 74% and for  $U_{10N} > 17 \text{ m s}^{-1}$  it is at 92%. Analysis of a very small number of visible images of the sea surface taken under hurricanes equally implied that  $W$  remains near constant for  $U_{10} > 24 \text{ m s}^{-1}$  (Holthuijsen et al. 2012). Note that under high wind speeds, streaks of foam and especially spray dominate and Holthuijsen et al. (2012) did not include streaks in their  $W$  estimate making it more representative of the active whitecap coverage than the total coverage considered here. Wide spread spray coverage at high wind speed may render whitecap and streak detection more



difficult in imagery. There may therefore be a practical upper wind speed limit to the current image analysis technique.

The datasets analyzed here display a weaker wind speed dependence than most previous studies, except for Salisbury et al. (2013). This weak wind speed dependence of  $W$  may be attributed to the low sea surface temperatures, averaging around 5-8°C, in which most of the measurements were taken. Only during the last station during HiWinGS did temperature exceed 10°C while surface water temperatures during SO GasEX did not exceed 14°C. Early work by Monahan and O'Muircheartaigh (1986) provided evidence of a weaker dependence of  $W$  on  $U$  for SSTs of 16°C compared to 32°C, but the increase of  $W$  with SST at a given wind speed was found to be modest. They analyzed 5 datasets including that collected by Bortkovskii (1987) which displays a strong positive dependence of  $W$  on SST and a near linear dependence of  $W$  on wind speed for SST less than 3°C. Monahan and O'Muircheartaigh (1986) argued that the water temperature will impact the exponent of the  $W(U)$  power-law and suggested that for SSTs around 10°C the exponent is around 2, while for SSTs warmer than 22°C the exponent is greater than 3. The weaker wind speed dependence in cold waters is reflected in the latitudinal variation of the dependence of  $W$  on  $U$  shown by Monahan et al. (2015) which is supported by Salisbury et al. (2014) who demonstrated that using a power-law wind speed dependence with an exponent of 3.41 leads to overestimation of  $W$  at high latitudes. Wu (1988) suggested that rather than affecting the exponent, temperature affects  $a$ , the slope of the power-law Eq. (2), though no systematic trends were found. It was further argued that all coefficients of the power-law vary with temperature, with the strongest temperature dependence is in the exponent (Albert et al. 2016). Cold waters suppress the rate of breaking, but increase the lifetime of bubbles and foam

patches thus having the potential to enhance or reduce  $W$  (Bortkovskii and Novak, 1993). Opposite trends in temperature dependence of air entrainment have been found in laboratory studies (Hwang et al. 1991, Slater et al. 2014, Callaghan et al. 2014). As individual field campaigns rarely sample a wide range of environmental parameters, it is essential to compile all existing data to detect trends and caution is advisable in determining trends from reduced datasets.

Continued improvement of whitecap parameterizations requires consideration of more than wind speed, specifically including statistics of the variable wave field. This motivated the concurrent measurement of whitecaps, winds, and wave field during SO GasEx and HiWinGS. Purely wave-dependent parameterizations that express  $W$  as a function of wave steepness or mean square slope within the equilibrium range do not give improved results over the wind-speed-only parameterizations. Nor does the wave age parameterization provide a better fit. The wave-wind Reynolds number based parameterizations show tighter correlations and better inter-dataset agreement than wave age and wave-only parameterizations. More wind and sea state conditions should be sampled to establish if there are, if any, limitations to these relationships. The breaking Reynolds number captures more of the variability in individual datasets, but  $R_B$  displays less inter-dataset agreement. Reynolds number functions have also been shown to provide better models of sea-spray aerosol fluxes than wind speed alone, with  $R_H$  explaining twice as much of total variance in direct measurements (Norris et al. 2013). While the Reynolds numbers have been typically computed using the friction velocity, the HiWinGS and SO GasEx data suggest that using the neutral 10 m wind speed lead to similar fit statistics for  $W$ .

Energy weighted or mean statistics ( $f_m$ ,  $H_m$ ,  $k_m$  and  $c_m$ ) are regularly chosen as being more representative of the breaking waves rather than peak statistics ( $f_p$ ,  $H_p$ ,  $k_p$  and  $c_p$ ) which often correspond to the swell in multimodal spectra (Sutherland and Melville, 2015). Schwendeman and Thomson (2015b) show that mean statistics are better predictors for  $W$  parameterizations further encouraging their use. The use of energy-weighted statistics of the wind-sea partition was motivated by the observation that most whitecaps are associated with waves even shorter than the mean (Gemmrich et al. 2008). This study, however, only suggests marginal improvement of fit statistics using mean wave field statistics.

As stated in the introduction,  $mss$  is computed over the equilibrium range. The existence of such a range, where sources and sinks are in balance was postulated by Phillips (1985). Based on measurements by Toba (1973), Phillips (1985) proposed an analytical expression for the energy spectrum within that range which is characterized by a  $f^{-4}$  spectral shape. Bounds for the equilibrium range were later suggested by Donelan (1985) as  $1.5f_p$  and  $3.5f_p$ . The upper bounds however seemed to be dictated by the highest frequency resolved by the measurements rather than the end of the range in which the spectrum is proportional to  $f^{-4}$ . Indeed, the equilibrium range was found to extend further: up to  $6f_p$  (Toba, 1973) or 0.35 to 0.4 Hz in Thomson et al. (2013) for  $f_p$  generally less than 0.1 Hz. Furthermore, the upper limit of the equilibrium range is not always easily detectable with no visible shift in slope of  $E(f)$  at the transition between the equilibrium and the saturation ranges.

The SO GasEx and HiWinGS datasets suggest that for multimodal spectra, particularly when the winds increase and wind-seas start appearing,  $1.5f_p < f < 3.5f_p$  incorporates the wind sea peak,

while  $\sqrt{2}f_m \leq f \leq \sqrt{5}f_m$  usually falls beyond the wind-sea peak. This is illustrated in Figure 7d. What is more, the equilibrium range defined in terms of  $f_m$ , also extends to higher frequencies, and its upper limit falls within those observed by Thomson et al. (2013). Determining the equilibrium range based on sections of the spectra beyond  $f_p$  that most closely decays as  $f^4$  led to highly variable results with little agreement between WW3 and the waverider. The  $mss$  computed over that range showed less correlation with  $W$  than the  $mss$  computed over  $\sqrt{2}f_m \leq f \leq \sqrt{5}f_m$ .

Finally, alignment of the swell and the wind sea was considered during the analysis by differentiating between periods of pure wind sea and pure swell as well as following, cross, and counter swell as defined in Sugihara et al. (2007). This analysis did not, however, result in distinct trends for the different alignments and is consequently not shown here.

## 6 Conclusion

Analysis of visible imagery, flux and wave data collected during SO GasEx and HiWinGS allowed for evaluation of existing whitecap coverage parameterizations. Considering the two datasets separately and computing best fits for each individually facilitates critical assessment of the parameterizations discussed in this study, which are further verified by comparison to published parameterizations. Based on this work and recent studies reviewed herein, it is apparent that wind speed only parameterizations show very little scatter for winds above  $10 \text{ m s}^{-1}$  and are able to capture the observed variability of  $W$  well. The neutral wind speed or friction velocity should be used for those parameterizations. Of all the wave-only, and wind and wave

dependent parameterizations tested here, the wave-wind Reynolds number parameterizations appear to be the most universally applicable ones as suggested by the close agreement between the best fits determined from the individual and combined datasets which are further in good agreement with those of Goddijn-Murphy et al. (2011) and Scanlon and Ward (2016). Although wave-wind Reynolds number parameterizations capture somewhat less of the observed variability in  $W$ , they are in closer agreement to previous studies than wind-only parameterizations. When wave field statistics are readily available, wave-wind Reynolds number parameterizations should be used. Such statistics do not have to be derived from directional spectra as separating wind seas from swell does not appear to yield significantly better representation of  $W$ . Results from this study do not support a more complex multi-parameter whitecap coverage model based on non-dimensional scaling.

## 7 Acknowledgements

This work was funded by the National Science Foundation (Grants OCE-0647667, OCE-1537890, AGS-1036062, AGS-1036006, AGS-1444294), the National Oceanic and Atmospheric Administration (Grant NA07OAR4310094), and the Natural Environment Research Council (grant NE/J020893/1). The authors would like to thank the anonymous reviewers for thoroughly and critically evaluating the manuscript. They are also grateful to the crew of the *R/V Knorr* for supporting us while chasing storms and that of the NOAA ship *Ronald H. Brown* for their support during SO GasEx. Data from this cruise will be uploaded on to the NOAA FTP server and made publicly available. This is Lamont-Doherty Earth Observatory contribution number XXXX.

## 8 References

- Albert, M. F. M. A., M. D. Anguelova, A. M. M. Manders, M. Schaap, and G. de Leeuw (2016), Parameterization of oceanic whitecap fraction based on satellite observations, *Atmos. Chem. Phys.*, **16**(21), 13725-13751.
- Andreae, M. O., and D. Rosenfeld, 2008: Aerosol–cloud–precipitation interactions. Part 1. The nature and sources of cloud-active aerosols. *Earth-Science Reviews*, **89**, 13-41.
- Anguelova, M. D., and F. Webster, 2006: Whitecap coverage from satellite measurements: A first step toward modeling the variability of oceanic whitecaps. *J. Geophys. Res.*, **111**, doi:10.1029/2005JC003158.
- Asher, W. E., and R. Wanninkhof, 1998: The effect of bubble-mediated gas transfer on purposeful dual-gaseous tracer experiments. *Journal of Geophysical Research*, **103**, 10555-10560.
- Banner, M. L., J. R. Gemmrich, and D. M. Farmer, 2002: Multiscale measurements of ocean wave breaking probability. *J. Phys. Oceanogr.*, **32**, 3364-3375.
- Blanchard, D. C., 1963: The electrification of the atmosphere by particles from bubbles in the sea. *Progress in Oceanography*, **1**, 73-202.

- , 1983: The Production, Distribution, and Bacterial Enrichment of the Sea-Salt Aerosol. *Air-Sea Exchange of Gases and Particles*, P. S. Liss, and W. G. N. Slinn, Eds., Springer Netherlands, 407-454.
- Blomquist, B. W., C. W. Fairall, B. J. Huebert, D. J. Kieber, and G. R. Westby, 2006: DMS sea-air transfer velocity: Direct measurements by eddy covariance and parameterization based on the NOAA/COARE gas transfer model. *Geophysical Research Letters*, **33**, Art. No. L07601.
- Bobak, J. P., W. E. Asher, D. J. Dowgiallo, and M. D. Angelova, 2011: Aerial Radiometric and Video Measurements of Whitecap Coverage. *IEEE Transactions on Geoscience and Remote Sensing*, **49**, 2183-2193.
- Bortkovskii, R. (1987), Air-Sea Exchange of Heat and Moisture During Storms, 193 pp., Springer, New York
- Bortkovskii, R. S., and V. A. Novak (1993), Statistical dependencies of sea state characteristics on water temperature and wind-wave age, *Journal of Marine Systems*, **4**(2), 161-169.
- Bouguet, J.-Y., cited 2016: Camera Calibration Toolbox for Matlab
- Callaghan, A. H., and M. White, 2009: Automated processing of sea surface images for the determination of whitecap coverage. *Journal of Atmospheric and Oceanic Technology*, **26**, 383-394.
- Callaghan, A. H., G. B. Deane, and M. D. Stokes, 2016: Laboratory air-entraining breaking waves: Imaging visible foam signatures to estimate energy dissipation, *Geophys. Res. Lett.*, **43**, 11,320–11,328, doi: 10.1002/2016GL071226
- Callaghan, A.H., Stokes, M.D., and Deane, G.B., 2014: The effect of water temperature on air entrainment, bubble plumes, and surface foam in a laboratory breaking-wave analog. *J. Geophys. Res. Atmos.*, **119**, 7463-7482.
- Callaghan, A. H., G. B. Deane, and M. D. Stokes, 2008a: Observed physical and environmental causes of scatter in whitecap coverage values in a fetch-limited coastal zone. *J. Geophys. Res.*, **113**, doi:10.1029/2007JC004453.
- Callaghan, A. H., G. d. Leeuw, L. Cohen, and C. D. O'Dowd, 2008b: Relationship of oceanic whitecap coverage to wind speed and wind history. *Geophys. Res. Lett.*, **35**, doi:10.1029/2008GL036165.
- Cavaleri, L., B. Fox-Kemper, and M. Hemer, 2012: Wind Waves in the Coupled Climate System. *Bulletin of the American Meteorological Society*, **93**, 1651-1661.
- Cavaleri, L., and Coauthors, 2007: Wave modelling – The state of the art. *Progress in Oceanography*, **75**, 603-674.
- Cifuentes-Lorenzen, A., J. B. Edson, C. J. Zappa, and L. Bariteau, 2013: A multi-sensor comparison of ocean wave frequency spectra from a research vessel during the Southern Ocean Gas Exchange Experiment. *J. Atmos. Oceanic Tech.*, **30**, 2907-2925.
- Cunliffe, M and O. Wurl, 2014: Guide to best practices to study the ocean's surface. Occasional Publications of the Marine Biological Association of the United Kingdom, Plymouth, UK. 118 pp.

847 de Leeuw, G., and Coauthors, 2011: Production flux of sea spray aerosol. *Rev. Geophys.*, **49**,  
848 doi:10.1029/2010RG000349.

849 Donelan, M. A. (1985), Directional Spectra of Wind-Generated Waves, *Philosophical*  
850 *transactions of the Royal Society of London. Series A: Mathematical, physical, and*  
851 *engineering sciences*, *315*(1534), 509-562.

852 Edson, J. B., A. A. Hinton, K. E. Prada, J. E. Hare, and C. W. Fairall, 1998: Direct covariance  
853 flux estimates from mobile platforms at sea. *J. Atmos. Oceanic Tech*, **15**, 547 - 562.

854 Edson, J. B., C. J. Zappa, J. Ware, W. R. McGillis, and J. E. Hare, 2004: Scalar flux profile  
855 relationships over the open ocean. *J Geophys. Res.*, **109**, C08S09.

856 Edson, J. B., and Coauthors, 2011: Direct covariance measurement of CO<sub>2</sub> gas transfer velocity  
857 during the 2008 Southern Ocean Gas Exchange Experiment: Wind speed dependency.  
858 *Journal of Geophysical Research – Oceans*, **116**, C00F10.

859 Edson, J. B., and Coauthors, 2013: On the exchange of momentum over the open ocean. *Journal*  
860 *of Physical Oceanography*, **43**, 1589-1610.

861 Fairall, C. W., E. F. Bradley, J. E. Hare, A. A. Grachev, and J. B. Edson, 2003: Bulk  
862 parameterization of air-sea fluxes: Updates and verification for the COARE algorithm. *J.*  
863 *Climate*, **16**, 571-591.

864 Fairall, C. W., and Coauthors, 2011: Implementation of the Coupled Ocean-Atmosphere  
865 Response Experiment flux algorithm with CO<sub>2</sub>, dimethyl sulfide, and O<sub>3</sub>. *J. Geophys. Res.*,  
866 **116**, doi:10.1029/2010JC006884.

867 Frew, N. M., 1997: The role of organic films in air-sea gas exchange. *The Sea Surface and*  
868 *Global Change*, P. S. Liss, and R. A. Duce, Eds., Cambridge University Press, 121-172.

869 Frouin, R., S. F. Iacobellis, and P. Y. Deschamps, 2001: Influence of oceanic whitecaps on the  
870 Global Radiation Budget. *Geophysical Research Letters*, **28**, 1523-1526.

871 Gaiser, P. W., and Coauthors, 2004: The WindSat spaceborne polarimetric microwave  
872 radiometer: Sensor description and early orbit performance. *Geoscience and Remote*  
873 *Sensing, IEEE Transactions on*, **42**, 2347-2361.

874 Garrett, W. D., 1967: Stabilization of air bubbles at the air-sea interface by surface active  
875 material, *Deep Sea Research*, **14**, 661-672.

876 Gemmrich, J. R., M. L. Banner, and C. Garrett, 2008: Spectrally resolved energy dissipation and  
877 momentum flux of breaking waves. *Journal of Physical Oceanography*, **38**, 1296–1312,  
878 doi:10.1175/ 2007JPO3762.1.

879 Goddijn-Murphy, L., D. K. Woolf, and A. H. Callaghan, 2011: Parameterizations and algorithms  
880 for oceanic whitecap coverage. *Journal of Physical Oceanography*, **41**, 742-756.

881 Gordon, H. R., and M. Wang, 1994: Retrieval of water-leaving radiance and aerosol optical  
882 thickness over the oceans with SeaWiFS: a preliminary algorithm. *Applied Optics*, **33**, 443-  
883 452.

884 Guan, C., W. Hu, J. Sun, and R. Li, 2007: The whitecap coverage model from breaking  
885 dissipation parametrizations of wind waves. *Journal of Geophysical Research: Oceans*,  
886 **112**, C05031.

887 Hanson, J. L., and O. M. Phillips, 1999: Wind sea growth and dissipation in the open ocean.  
888 *Journal of Physical Oceanography*, **29**, 1633-1648.



- Hanson, J. L., and O. M. Phillips, 2001: Automated Analysis of Ocean Surface Directional Wave Spectra. *Journal of Atmospheric and Oceanic Technology*, **18**, 277-293.
- Hasselmann, S., K. Hasselmann, J. H. Allender, and T. P. Barnett, 1985: Computations and Parameterizations of the Nonlinear Energy Transfer in a Gravity-Wave Spectrum. Part II: Parameterizations of the Nonlinear Energy Transfer for Application in Wave Models. *Journal of Physical Oceanography*, **15**, 1378-1391.
- Haywood, J. M., V. Ramaswamy, and B. J. Soden, 1999: Tropospheric Aerosol Climate Forcing in Clear-Sky Satellite Observations over the Oceans. *Science*, **283**, 1299-1303.
- Ho, D. T., C. L. Sabine, D. Hebert, D. S. Ullman, R. Wanninkhof, R. C. Hamme, P. G. Strutton, B. Hales, J. B. Edson, and B. R. Hargreaves 2011: Southern Ocean Gas Exchange Experiment: Setting the stage, *Journal of Geophysical Research - Oceans*, **116**(C4), C00F08, doi: 10.1029/2010JC006852.
- Holland, K. T., R. A. Holman, T. C. Lippmann, J. Stanley, and N. Plant, 1997: Practical use of video imagery in nearshore oceanographic field studies. *IEEE Journal of Oceanic Engineering*, **22**, 81-92.
- Holthuijsen, L.H., Powell, M.D. and Pietrzak, J.D., 2012: Wind and waves in extreme hurricanes. *Journal of Geophysical Research: Oceans*, **117**, C09003, doi:10.1029/2012JC007983.
- Hwang, P. A, Y. Poon, and J. Wu 1991: Temperature effects on generation and entrainment of bubbles induced by a water jet. *J. Phys. Oceanogr.*, **21**, 1602-1605.
- Jessup, A. T., C. J. Zappa, M. R. Loewen, and V. Hesany, 1997: Infrared remote sensing of breaking waves. *Nature*, **385**, 52-55.
- Johnson, D., cited 2016: DIWASP, a directional wave spectra toolbox for MATLAB®: User Manual. Research Report WP-1601-DJ (V1.1)
- Kleiss, J. M., and W. K. Melville, 2010: Observations of wave breaking kinematics in fetchlimited seas. *J. Phys. Oceanogr.*, **40**, 2575-2604.
- Komen, G. J., L. Cavaleri, M. A. Donelan, K. Hasselmann, S. Hasselmann, and P. A. E. M. Janssen, 1994: *Dynamics and Modelling of Ocean Waves*. Cambridge University Press, Cambridge, 532 pp.
- Kraan, G., W. A. Oost, and P. A. E. M. Janssen, 1996: Wave Energy Dissipation by Whitecaps. *Journal of Atmospheric and Oceanic Technology*, **13**, 262-267.
- Kuik, A. J., G. P. v. Vledder, and L. H. Holthuijsen (1988), A Method for the Routine Analysis of Pitch-and-Roll Buoy Wave Data, *Journal of Physical Oceanography*, **18**(7), 1020-1034.
- Lafon, C., J. Piazzola, P. Forget, and S. Despiau, 2007: Whitecap coverage in coastal environment for steady and unsteady wave field conditions. *Journal of Marine Systems*, **66**, 38-46.
- Lafon, C., J. Piazzola, P. Forget, O. Le Calve, and S. Despiau, 2004: Analysis of the Variations of the Whitecap Fraction as Measured in a Coastal Zone. *Boundary-Layer Meteorology*, **111**, 339-360.
- Lund, B., C. J. Zappa, H. C. Graber, and A. Cifuentes-Lorenzen, 2016: Shipboard Wave Measurements in the Southern Ocean. *Journal of Atmospheric and Oceanic Technology*, **in revision**.
- Melville, W. K., 1996: The role of surface-wave breaking in air-sea interaction. *Annual Review of Fluid Mechanics*, **28**, 279-321.
- Mironov, A. S., and V. A. Dulov, 2008: Detection of wave breaking using sea surface video records. *Meas. Sci. Technol.*, **19**, doi:10.1088/0957-0233/1019/1081/015405.
- Monahan, E. C., G. Hooker, and C. J. Zappa (2015), The Latitudinal Variation in the Wind-Speed Parameterization of Oceanic Whitecap Coverage; Implications for Global Modelling

- of Air-Sea Gas Flux and Sea Surface Aerosol Generation, in *95<sup>th</sup> Annual American Meteorological Meeting*, edited, Phoenix, AZ, USA.
- Monahan, E. C., 1971: Oceanic Whitecaps. *Journal of Physical Oceanography*, **1**, 139-144.
- Monahan, E. C., and M. C. Spillane, 1984: The role of oceanic whitecaps in air-sea gas exchange. *Gas Transfer at Water Surfaces*, W. Brutsaert, and G. H. Jirka, Eds., D. Reidel, 495-503.
- Monahan, E. C., and I. G. O'Muircheartaigh, 1986: Whitecaps and the passive remote sensing of the ocean surface. *International Journal of Remote Sensing*, **7**, 627-642.
- Mori, N., T. Suzuki, and S. Kakuno, 2007: Noise of Acoustic Doppler Velocimeter Data in Bubbly Flows. *Journal of Engineering Mechanics*, **133**, 122-125.
- Myrhaug, D., and L. E. Holmedal, 2008: Effects of wave age and air stability on whitecap coverage. *Coastal Engineering*, **55**, 959-966.
- Nayar, K. G., M. H. Sharqawy, L. D. Banchik, and J. H. Lienhard V, 2016: Thermophysical properties of seawater: A review and new correlations that include pressure dependence. *Desalination*, **390**, 1-24.
- Norris, S. J., I. M. Brooks, and D. J. Salisbury, 2013: A wave roughness Reynolds number parameterization of the sea spray source flux. *Geophysical Research Letters*, **40**, 4415-4419.
- Paget, A. C., M. A. Bourassa, and M. D. Angelova 2015: Comparing in situ and satellite-based parameterizations of oceanic whitecaps. *J. Geophys. Res. Oceans*, **120**, 2826–2843, doi:10.1002/2014JC010328.
- Phillips, O. M., 1985: Spectral and statistical properties of the equilibrium range in wind-generated gravity waves. *Journal of Fluid Mechanics*, **156**, 505-531.
- Randolph, K., and Coauthors, 2016: Novel methods for optically measuring whitecaps under natural wave breaking conditions in the Southern Ocean. *Journal of Atmospheric and Oceanic Technology*, **0**, null.
- Salisbury, D. J., D. Angelova, and I. M. Brooks , 2014: Global distribution and seasonal dependence of satellite-based whitecap fraction, *Geophysical research letters*, *41*(5), 1616-1623.
- Saha, S., and Coauthors, 2010: The NCEP Climate Forecast System Reanalysis. *Bulletin of the American Meteorological Society*, **91**, 1015-1057.
- Salisbury, D. J., M. D. Angelova, and I. M. Brooks, 2013: On the variability of whitecap fraction using satellite-based observations. *Journal of Geophysical Research: Oceans*, **118**, 6201-6222.
- Scanlon, B., and B. Ward, 2013: Oceanic wave breaking coverage separation techniques for active and maturing whitecaps. *Methods in Oceanography*, **8**, 1-12.
- , 2016: The influence of environmental parameters on active and maturing oceanic whitecaps. *Journal of Geophysical Research: Oceans*, **121**, 3325-3336.
- Schwendeman, M., and J. Thomson, 2015a: A Horizon-Tracking Method for Shipboard Video Stabilization and Rectification. *Journal of Atmospheric and Oceanic Technology*, **32**, 164-176.
- , 2015b: Observations of whitecap coverage and the relation to wind stress, wave slope, and turbulent dissipation. *Journal of Geophysical Research: Oceans*, **120**, 8346-8363.
- Schwendeman, M., J. Thomson, and J. R. Gemmrich, 2014: Wave breaking and dissipation in a young wind sea. *Journal of Physical Oceanography*, **44**, 104-127.

- Sharqawy, M. H., J. H. Lienhard, and S. M. Zubair, 2010: Thermophysical properties of seawater: a review of existing correlations and data. *Desalination and Water Treatment*, **16**, 354-380.
- Salter, M. E., E. D. Nilsson, A. Butcher, and M. Bilde 2014: On the seawater temperature dependence of the sea spray aerosol generated by a continuous plunging jet. *J. Geophys. Res.*, **119**, 9052–9072, doi: 10.1002/2013JD021376.
- Spillane, M., E. C. Monahan, P. Bowyer, D. Doyle, and P. J. Staben, 1986: Whitecaps and global fluxes. *Oceanic Whitecaps*, Springer, 209-218.
- Stokes, G. G., 1880: Considerations relative to the greatest height of oscillatory irrotational waves which can be propagated without change of form. *Mathematical and physical papers*, **1**, 225-228.
- Sugihara, Y., H. Tsumori, T. Ohga, H. Yoshioka, and S. Serizawa, 2007: Variation of whitecap coverage with wave-field conditions. *Journal of Marine Systems*, **66**, 47–60.
- Sutherland, P., and W. K. Melville, 2015: Field measurements of surface and near-surface turbulence in the presence of breaking waves. *Journal of Physical Oceanography*, **45**, 943–965, doi:10.1175/JPO-D-14-0133.1.
- Thomson, J., E. D'Asaro, M. Cronin, W. Rogers, R. Harcourt, and A. Shcherbina, 2013: Waves and the equilibrium range at Ocean Weather Station P, *Journal of Geophysical Research: Oceans*, **118**(11), 5951-5962.
- Toba, Y., and M. Koga, 1986: A Parameter Describing Overall Conditions of Wave Breaking, Whitecapping, Sea-Spray Production and Wind Stress. *Oceanic Whitecaps*, E. Monahan, and G. Niocaill, Eds., Springer Netherlands, 37-47.
- Toba, Y. 1973: Local balance in the air-sea boundary processes, *Journal of Oceanography*, **29**(5), 209-220.
- Tolman, H. L., 2009: User manual and system documentation of WAVEWATCH III TM version 3.14, Tech. Note. MMAB No. 276.
- Tolman, H. L., and D. Chalikov, 1996: Source Terms in a Third-Generation Wind Wave Model. *Journal of Physical Oceanography*, **26**, 2497-2518.
- Tolman, H. L., B. Balasubramanian, L. D. Burroughs, D. V. Chalikov, Y. Y. Chao, H. S. Chen, and V. M. Gerald, 2002: Development and Implementation of Wind-Generated Ocean Surface Wave Models at NCEP. *Weather and Forecasting*, **17**, 311-333.
- Woolf, D. K., 1997: Bubbles and their role in air–sea gas exchange. *The Sea Surface and Global Change*, PS Liss, and R. Duce, Eds., Cambridge Univ Press, Cambridge, UK, 173-206.
- , 2005: Parameterization of gas transfer velocities and sea-state-dependent wave breaking. *Tellus*, **57B**, 87-94.
- Woolf, D. K., and Coauthors, 2007: Modelling of bubble-mediated gas transfer: Fundamental principles and a laboratory test. *Journal of Marine Systems*, **66**, 71-91.
- Wu, J., 1988: Variations of whitecap coverage with wind stress and water temperature. *Journal of Physical Oceanography*, **18**, 1448-1453.
- Zappa, C. J., M. L. Banner, J. R. Gemmrich, H. Schultz, R. P. Morison, D. A. LeBel, and T. Dickey, 2012: An overview of sea state conditions and air-sea fluxes during RaDyO. *Journal of Geophysical Research – Oceans*, **117**, C00H19.
- Zhao, D., and Y. Toba, 2001: Dependence of whitecap coverage on wind and wind-wave properties. *Journal of Oceanography*, **57**, 603-616.

## 1026 9 List of Tables

1027	Table 1 – Wind speed only parameterizations of whitecap coverage determined in this study. Fits	
1028	were computed from the binned averages, but statistics are reported with respect to the	
1029	hourly estimates. Note that $W$ is expressed as a percentage as is its rmse. The correlation	
1030	coefficients were computed in log space to give equal weight to the whitecap data	
1031	across several orders of magnitude.....	50
1032	Table 2 – Wave steepness and mean square slope parameterizations of whitecap coverage (%)	
1033	determined in this study. Wind-sea only statistics are denoted by a ‘ws’ subscript. Fits	
1034	and data computed as for Table1.....	51
1035	Table 3 – Wave age parameterizations of whitecap coverage (%) determined in this study. Wind-	
1036	sea only statistics are denoted by a ‘ws’ subscript. Fits and data computed as for Table1.	
1037	.....	52
1038	Table 4 – Wave-wind Reynolds number parameterizations of whitecap coverage (%) determined	
1039	in this study. Wind-sea only statistics are denoted by a ‘ws’ subscript. Fits and data	
1040	computed as for Table1. ....	53
1041	Table 5 – Breaking-wave Reynolds number parameterizations of whitecap coverage (%)	
1042	determined in this study. Wind-sea only statistics are denoted by a ‘ws’ subscript. Fits	
1043	and data computed as for Table1.....	54
1044	Table 6 – Results of the linear regression $\log_{10}W = \log_{10}a + a\log_{10}cmu * $	
1045	$+ \beta \log_{10}Hskm2 + \gamma \log_{10}Hmu */vw$ .....	55
1046		

## 1047 10 List of Figures

1048	Figure 1 – Parameterizations of Whitecap coverage ( $W$ ) as a function of wind speed ( $U_{10}$ )	
1049	published since 2004 (see APPENDIX A).....	56
1050	Figure 2 – Ships tracks a) SO GasEx and b) HiWinGS; the color code shows the significant wave	
1051	height [m] .....	57
1052	Figure 3 – Wind speed time series; a) for SO GasEx, and b) for HiWinGS. The gray shading	
1053	represents periods when the ship was on station during HiWinGS. The red lines	
1054	correspond to periods of visible imagery recording. ....	58
1055	Figure 4 – Steps of the image processing: a) raw image, b) lens calibration, c) roll and yaw	
1056	correction, d) projection based on incidence angle and height of camera assuming flat	
1057	surface and e) thresholded and projected image.....	59
1058	Figure 5 – Time series of the normalized cumulative whitecap coverage $W_{CA_{norm}}$ color-coded by	
1059	wind speed (a,c) and wave age (b,d) for SO GasEx (a,b) and HiWinGS (c,d). The black	
1060	solid and dashed lines represent the one and two standard deviations bounds computed	
1061	from $W_{CA_{norm}}$ of the respective datasets for a given time. Non-converging $W_{CA_{norm}}$ are	
1062	represented by lines that fall outside of the 2 standard deviations bound after 15 minutes	
1063	for more than 3 minutes.....	60
1064	Figure 6 – time series of the a) incidence and b) roll angles measured by the IMU (orange) and	
1065	determined by the horizon tracking toolbox (blue). ....	61
1066	Figure 7 – WAMOS measurements taken during SO GasEx: a) the spectragram, b) an example	
1067	of a directional wave spectra , c) the time series of the significant wave height computed	
1068	from the total spectrum and the wind-sea partition, and d) the omnidirectional wave	
1069	spectra computed from b) with vertical lines depicting the peak and mean frequencies	
1070	and horizontal lines showing equilibrium ranges based on the peak frequency, the mean	
1071	frequency and portion of the spectra proportional to the frequency to the power -4. ....	62
1072	Figure 8– Wave field measurements and model hind cast for HiWinGS. a) and c) show	
1073	spectragrams from the waverider and from the WAVEWATCH-III® hind cast,	
1074	respectively. Examples of directional wave spectra from the waverider, and from the	
1075	WAVEWATCH-III® hind cast corresponding to the same time are shown in b) and d).	
1076	The time series of the significant wave heights computed from the total spectrum and	
1077	the wind-sea partition of both the waverider and the model hind cast is shown in e), and	
1078	d) depicts the omnidirectional wave spectra computed from d) with vertical lines	
1079	depicting the peak and mean frequencies and horizontal lines showing equilibrium	
1080	ranges based on the peak frequency, the mean frequency and portion of the spectra	
1081	proportional to the frequency to the power -4. The grey shading in a), b), and e)	
1082	indicates periods when the <i>R/V Knorr</i> was on station. ....	63
1083	Figure 9 – Whitecap coverage ( $W$ ) as a function of a) the 10 m neutral wind speed ( $U_{10N}$ ) and b)	
1084	the friction velocity ( $u_*$ ). The small light red dots show the hourly averaged whitecap	
1085	coverage computed from the HiWinGS dataset, while the small blue squares are the 30	
1086	minute averaged whitecap coverage computed from the SO GasEx dataset. The blue	
1087	squares and red circles show averages of 7 neighboring points for SO GasEx and	

1088	HiWinGS, respectively. These are used to compute the best fit shown by the dashed red	
1089	and blue lines. The dark purple lines show the best fits to the binned combined data.	
1090	The gray lines correspond to the parameterizations summarized in APPENDIX A and	
1091	APPENDIX D .	64
1092	Figure 10 – Whitecap coverage ( $W$ ) as a function of a) mean wave steepness and b) mean square	
1093	slope normalized by the directional spread and frequency bandwidth. The small light	
1094	red dots show the hourly averaged whitecap coverage computed from the HiWinGS	
1095	dataset, while the small blue squares are the 30 minute averaged whitecap coverage	
1096	computed from the SO GasEx dataset. The blue squares and red circles show averages	
1097	of 7 neighboring points for SO GasEx and HiWinGS, respectively. These are used to	
1098	compute the best fit shown by the dashed red and blue lines. The dark purple lines show	
1099	the best fits to the binned combined data. The black lines correspond to	
1100	parameterizations of Schwendeman and Thomson (2015b).	65
1101	Figure 11 – Whitecap coverage ( $W$ ) as a function of wave age a) $c_p/u_*$ , b) $c_p/u_*$ using the wind-	
1102	sea spectral peak, c) $c_p/U_{10N}$ using the wind-sea spectral peak, and d) $c_p/$	
1103	$U_{10N}$ .whitecap coverage. The small light red dots show the hourly averaged whitecap	
1104	coverage computed from the HiWinGS dataset, while the small blue squares are the 30	
1105	minute averaged whitecap coverage computed from the SO GasEx dataset. The blue	
1106	squares and red circles show averages of 7 neighboring points for SO GasEx and	
1107	HiWinGS, respectively. These are used to compute the best fit shown by the dashed red	
1108	and blue lines. The dark purple lines shows the best fit to the binned combined data.	
1109	The black and gray lines correspond to the parameterizations summarized in	
1110	APPENDIX C.	66
1111	Figure 12 – Whitecap coverage ( $W$ ) as a function of a) wave-wind and b) breaking-wave	
1112	Reynolds number computed from the significant wave height and peak angular velocity	
1113	of the entire wave spectrum. The small light red dots show the hourly averaged	
1114	whitecap coverage computed from the HiWinGS dataset, while the small blue squares	
1115	are the 30 minute averaged whitecap coverage computed from the SO GasEx dataset.	
1116	The blue squares and red circles show averages of 7 neighboring points for SO GasEx	
1117	and HiWinGS, respectively. These are used to compute the best fit shown by the dashed	
1118	red and blue lines. The dark purple lines shows the best fit to the binned combined data.	
1119	The black and gray lines correspond to the parameterizations summarized in	
1120	APPENDIX B.	67
1121	Figure 13- Scatter plot of the measured whitecap coverage ( $W$ ) plotted against the multiple	
1122	parameter model: $W = a \left(\frac{c_m}{u_*}\right)^\alpha \left(\frac{H_m k_m}{2}\right)^\beta \left(\frac{H_m u_*}{v_w}\right)^\gamma$ . In black the 1:1 line.	68
1123	Figure 14- Scatter plots of the whitecap coverage ( $W$ ) estimated from the scaled and non-scales	
1124	imagery a) individual frames, and b) 20 minute averages.	69
1125		
1126		

1127    **11 List of Appendices**

1128	APPENDIX A – Parameterizations of whitecap coverage [%] as a function of wind speed (since	
1129	2004). Letters given in the second column are used as references in the legends in	
1130	Figure 1.....	46
1131	APPENDIX B – Parameterizations of whitecap coverage [%] as a function of breaking-wave and	
1132	wave-wind Reynolds numbers. Letters given in the second column are used as	
1133	references in the legends in Figure 11. ....	47
1134	APPENDIX C – Parameterizations of whitecap coverage [%] as a function of wave age. Letters	
1135	given in the second column are used as references in the legends in Figure 10.	48
1136	APPENDIX D – Parameterizations of whitecap coverage [%] as a function of the friction	
1137	velocity ( $u_*$ ). Letters given in the second column are used as references in the legends in	
1138	Figure 8b.....	49
1139		

1140 APPENDIX A – Parameterizations of whitecap coverage [%] as a function of wind speed (since 2004). Letters given in the second  
1141 column are used as references in the legends in Figure 1.



Reference		Formula	Wind speed range [m s <sup>-1</sup> ]	Sea state	Data Set
Scanlon and Ward (2016)	A	$W(U_{10}) = 7.84 \times 10^{-4}(U_{10N} - 2.56)^3$	$1 < U_{10} \leq 21$		Knorr11 & SOAP 2012
Schwendeman and Thomson (2015b)	A	$W(U_{10}) = 2.81 \times 10^{-3}(U_{10} - 3.87)^{2.76}$	$5.5 < U_{10} \leq 16$		North Pacific cruises 2012 & 2015
Salisbury et al. (2013)	A	$W_{10}(U_{10}) = 4.6 \times 10^{-3}U_{10}^{2.26}$	$2 < U_{10} \leq 20$		satellite W - 10 Ghz
	B	$W_{37}(U_{10}) = 3.97 \times 10^{-2}U_{10}^{1.59}$			satellite W - 37 Ghz
Goddijn-Murphy et al. (2011)	A	$W(U_{10}) = 15.9 \times 10^{-4}U_{10}^{2.7}$	$4.6 < U_{10} < 23.09$		MAP W; in situ winds
	B	$W(U_{10}) = 35.7 \times 10^{-4}(U_{10} - 3.83)^3$	$U_{10} < 11.5$		
	C	$W(U_{10}) = 46.9 \times 10^{-5}(U_{10} + 2.28)^3$	$U_{10} > 9.25$		
Callaghan et al. (2008a)	A	$W(U_{10}) = 4.66 \times 10^{-5}U_{10}^{3.95}$	$3.5 < U_{10} < 12$	mixed seas	Coastal site at Marthas Vineyard
	B	$W(U_{10}) = 2.99 \times 10^{-5}U_{10}^{3.95}$	$3.5 < U_{10} < 12$	swell dominated	
Callaghan et al. (2008b)	A	$W(U_{10}) = 3.18 \times 10^{-3}(U_{10} - 3.7)^3$	$4.6 < U_{10} \leq 11.25$		MAP campaign
	B	$W(U_{10}) = 4.82 \times 10^{-4}(U_{10} + 1.98)^3$	$9.25 < U_{10} \leq 23.09$		
Sugihara et al. (2007)	A	$W(U_{10}) = 8.04 \times 10^{-4}(U_{10} - 2.01)^3$	$4.37 < U_{10} < 16.35$	all	Shirahama observation tower
	B	$W(U_{10N}) = 8.57 \times 10^{-4}(U_{10N} - 1.34)^3$	$4.79 < U_{10N} < 16.57$	pure wind-sea	
	C	$W(U_{10N}) = 1.09 \times 10^{-3}(U_{10N} - 3.24)^3$	$4.79 < U_{10N} < 16.57$	other	
Lafon et al. (2007)	A	$W(U_{10}) = 8.1 \times 10^{-5}U_{10}^{3.88}$	$10 \leq U_{10} \leq 17.9$	stationary	EMMA Campaign Toulon-Hyeres bay
	B	$W(U_{10}) = 1.9 \times 10^{-4}U_{10}^{3.51}$		all	

1143 APPENDIX B – Parameterizations of whitecap coverage [%] as a function of breaking-wave and wave-wind Reynolds numbers.  
1144 Letters given in the second column are used as references in the legends in Figure 12.  
1145

Reference		Formula	Range	Data set and comments
Scanlon and Ward (2016)	B	$W(R_{H_a}) = 1.1 \times 10^{-10} R_{H_a}^{1.98}$ (log-log fit)	$10^4 < R_{H_a} < 2.5 \times 10^5$	Knorr11 & SOAP 2012
	C	$W(R_{H_a}) = 1.4 \times 10^{-5} R_{H_a}^{0.98}$		
	D	$W(R_{B_a}) = 8.9 \times 10^{-8} R_{B_a}^{1.61}$ (log-log fit)	$2.1 \times 10^2 < R_{B_a} < 7 \times 10^4$	
	E	$W(R_{B_a}) = 2.7 \times 10^{-5} R_{B_a}^{1.07}$		
Goddijn-Murphy et al. (2011)	D	$W(R_{H_w}) = 4.51 \times 10^{-6} R_{H_w}^{0.91}$	$2 \times 10^4 < R_{H_w} < 6 \times 10^6$	MAP W; in situ wind; ECMWF wave stats; $R_{H_{ww}}$ computed based on wind sea $H_s$
	E	$W(R_{H_w}) = 10.2 \times 10^{-7} R_{H_w}$	$2 \times 10^4 < R_{H_w} < 2.5 \times 10^5$	
	F	$W(R_{H_w}) = 1.53 \times 10^{-8} R_{H_w}^{1.34}$	$2 \times 10^4 < R_{H_w} < 2.5 \times 10^5$ ( $U_{10} < 8.6$ )	
	G	$W(R_{H_{ww}}) = 11.3 \times 10^{-7} R_{H_{ww}}$		
	H	$W(R_{B_a}) = 28.6 \times 10^{-5} R_{B_a}^{0.86}$	$3 \times 10^2 < R_{B_a} < 10^5$	
	I	$W(R_{B_a}) = 8.28 \times 10^{-7} R_{B_a}^{1.51}$	$3 \times 10^2 < R_{B_a} < 5 \times 10^3$ ( $U_{10} < 8.6$ )	
Lafon et al. (2007)	E	$W(R_{B_a}) = 3.7 \times 10^{-5} R_{B_a}^{1.1}$	$6 \times 10^3 < R_{B_a} < 3 \times 10^4$	EMMA Campaign Toulon-Hyeres bay
Lafon et al. (2004)	A	$W(R_{B_a}) = 3.2 \times 10^{-7} R_{B_a}^{1.64}$	$3 \times 10^3 < R_{B_a} < 2 \times 10^4$	FETCH
Zhao and Toba (2001)	A	$W(R_{H_a}) = 4.02 \times 10^{-5} R_{H_a}^{0.96}$	$10^2 \leq R_{H_a} \leq 5 \times 10^5$	wind-wave tunnel, coastal and other field data from six different studies
	B	$W(R_{B_a}) = 3.88 \times 10^{-5} R_{B_a}^{1.09}$	$10^2 \leq R_{B_a} < 10^5$	
Toba and Koga (1986)	A	$W(R_{B_a}) = 8.9 \times 10^{-5} R_{B_a}$	$5 \times 10^2 < R_{B_a} < 2 \times 10^4$	wind-wave tunnel & oceanographic tower

1146

1147 APPENDIX C – Parameterizations of whitecap coverage [%] as a function of wave age. Letters given in the second column are used  
1148 as references in the legends in Figure 11.

Reference	Formula	Range	Data sets
Scanlon and Ward (2016)	F $W\left(\frac{c_p}{U_{10}}\right) = 9.97 \left(\frac{c_p}{U_{10}}\right)^{-0.95}$	$1 \leq \frac{c_p}{U_{10}} \leq 6$	Knorr11 & SOAP 2012
Schwendeman and Thomson (2015b)	C $W\left(\frac{c_p}{u_*}\right) = 47 \left(\frac{c_p}{u_*}\right)^{-1.1}$	$8 < \frac{c_p}{u_*} < 29$	North Pacific cruises 2012 and 2015
	D $W\left(\frac{c_m}{U_{10}}\right) = 8.48 \times 10^{-1} \left(\frac{c_m}{U_{10}}\right)^{-3.53}$		
	E $W\left(\frac{c_m}{u_*}\right) = 9.33 \times 10^2 \left(\frac{c_m}{u_*}\right)^{-1.945}$	$18 < \frac{c_m}{u_*} < 52$	
Callaghan et al. (2008a)	C $W\left(\frac{c_p}{U_{10}}\right) = 3.11 \times 10^{-2} \left(\frac{c_p}{U_{10}}\right)^{-4.63}$	$0.5 \leq \frac{c_p}{U_{10}} \leq 1.7$	Coastal site at Marthas Vineyard
	D $W\left(\frac{c_p}{u_*}\right) = 1.81 \times 10^5 \left(\frac{c_p}{u_*}\right)^{-4.63}$	$15 \leq \frac{c_p}{u_*} \leq 48$	
Guan et al. (2007)	A $W\left(\frac{c_p}{u_*}\right) = 2.97 \times 10^2 \left(\frac{c_p}{u_*}\right)^{-2}$	$8 < \frac{c_p}{u_*} < 28$	FETCH
	B $W\left(\frac{c_p}{u_*}\right) = 2.82 \times 10^2 \left(\frac{c_p}{u_*}\right)^{-2}$	$8 < \frac{c_p}{u_*} < 32$	FETCH and Bohai Sea data sets
Lafon et al. (2007)	F $W\left(\frac{c_p}{U_{10}}\right) = 0.54 \times \left(\frac{c_p}{U_{10}}\right)^{-5.75}$	$0.67 \leq \frac{c_p}{U_{10}} < 1$	EMMA Campaign Toulon-Hyeres bay
	G $W\left(\frac{c_p}{U_{10}}\right) = \begin{cases} 70 \times \left(\frac{c_p}{U_{10}}\right)^{8.5} \\ 0.65 \times \left(\frac{c_p}{U_{10}}\right)^{-4.1} \end{cases}$	$0.52 \leq \frac{c_p}{U_{10}} \leq 0.69$ $0.69 < \frac{c_p}{U_{10}} < 1$	
Lafon et al. (2004)	B $W\left(\frac{c_p}{u_*}\right) = 210 \left(\frac{c_p}{u_*}\right)^{-1.75}$	$15 < \frac{c_p}{u_*} < 28$	FETCH
	C $W\left(\frac{c_p}{u_*}\right) = 2 \times 10^6 \left(\frac{c_p}{u_*}\right)^{-4.9}$	$8 < \frac{c_p}{u_*} < 28$	
	D $W\left(\frac{c_p}{u_*}\right) = -0.187 \times \left(\frac{c_p}{u_*}\right) + 5.2$	$8 < \frac{c_p}{u_*} < 28$	
Kraan et al. (1996)	A $W_A\left(\frac{c_p}{u_*}\right) = 96 \left(\frac{c_p}{u_*}\right)^{-2.08}$	$11 \leq \frac{c_p}{u_*} \leq 34$	ASGASEX & Meetpost Nooord-wijk coastal research platform

1149

1150

1151 APPENDIX D – Parameterizations of whitecap coverage [%] as a function of the friction velocity ( $u_*$ ). Letters given in the second  
 1152 column are used as references in the legends in Figure 9b.

Reference		Formula	Wind speed range [ $\text{m s}^{-1}$ ]	sea state conditions	Data Set
Schwendeman and Thomson (2015b)	B	$W(u_*) = 6.82(u_* - 1.39 \times 10^{-1})^{2.04}$	$0.2 < u_* \leq 0.75$		North Pacific cruises 2012 & 2015
Sugihara et al. (2007)	D	$W(u_*) = 9.53(u_* - 0.074)^3$	$0.212 < u_* < 0.67$		Shirahama observation tower
Lafon et al. (2007)	C	$W(u_*) = 10.2 \times u_*^{2.53}$	$0.33 \leq u_* \leq 0.8$	stationary	EMMA Campaign Toulon-Hyeres bay
	D	$W(u_*) = 7.78 \times u_*^{2.29}$		all	

1153

1154 Table 1 – Wind speed only parameterizations of whitecap coverage determined in this study. Fits  
1155 were computed from the binned averages, but statistics are reported with respect to the hourly  
1156 estimates. Note that  $W$  is expressed as a percentage as is its  $rmse$ . The correlation coefficients  
1157 were computed in log space to give equal weight to the whitecap data across several orders of  
1158 magnitude.

Experiment	best fit equation	range	$r^2$	$rmse$
HiWinGS	$W = 8.07 \times 10^{-2} (U_{10N} - 4.45)^{1.37}$	$5.46 \leq U_{10N} \leq 23.96 \text{ m s}^{-1}$	0.51	1.35
SO GasEx	$W = 2.31 \times 10^{-2} (U_{10N} - 4.20)^{2.03}$	$5.61 \leq U_{10N} \leq 15.82 \text{ m s}^{-1}$	0.34	0.96
Combined	$W = 7.38 \times 10^{-2} (U_{10N} - 4.23)^{1.42}$	$4.56 \leq U_{10N} \leq 25.10 \text{ m s}^{-1}$	0.48	1.22
HiWinGS	$W = 4.24(u_* - 0.14)^{1.10}$	$0.17 \leq u_* \leq 1.24 \text{ m s}^{-1}$	0.51	1.35
SO GasEx	$W = 5.84(u_* - 0.17)^{1.30}$	$0.21 \leq u_* \leq 0.77 \text{ m s}^{-1}$	0.16	1.00
Combined	$W = 4.32(u_* - 0.14)^{1.09}$	$0.15 \leq u_* \leq 1.24 \text{ m s}^{-1}$	0.37	1.24

1159

Table 2 – Wave steepness and mean square slope parameterizations of whitecap coverage (%) determined in this study. Wind-sea only statistics are denoted by a ‘ws’ subscript. Fits and data computed as for Table 1.

Predictor	Experiment	$a$	$n$	range	$r^2$	$rmse$
$mss$	HiWinGS	1.47E+04	1.63	1.43E-03 – 5.32E-03	0.16	1.61
	SO GasEx	5.40E+00	0.28	8.05E-04 – 4.59E-03	-0.11	1.32
	Combined	1.72E+02	0.82	6.48E-04 – 5.35E-03	-0.04	1.56
$mss_{ws}$	HiWinGS	4.42E+03	1.39	2.01E-03 – 6.84E-03	-0.08	1.64
	SO GasEx	2.81E+00	0.19	6.27E-04 – 3.80E-03	-0.13	0.72
	Combined	1.73E+03	1.22	3.87E-04 – 6.16E-03	0.00	1.54
$mss/\Delta\theta\Delta f$	HiWinGS	5.80E+01	1.18	1.21E-02 – 9.44E-02	0.28	1.49
	SO GasEx	5.96E+00	0.52	1.34E-02 – 7.71E-02	-0.19	1.33
	Combined	2.19E+01	0.84	8.11E-03 – 9.59E-02	0.02	1.49
$mss_{ws}/\Delta\theta\Delta f$	HiWinGS	5.95E+01	1.17	1.65E-02 – 1.16E-01	0.36	1.45
	SO GasEx	5.99E+00	0.58	1.84E-02 – 4.94E-02	-0.15	0.78
	Combined	4.99E+01	1.09	1.10E-02 – 9.55E-02	0.25	1.42
$H_s k_m/2$	HiWinGS	9.05E+06	4.16	1.34E-02 – 2.91E-02	0.21	1.54
	SO GasEx	1.91E+02	1.23	1.03E-02 – 2.06E-02	-0.19	1.30
	Combined	3.71E+03	2.02	8.83E-03 – 2.87E-02	0.05	1.48
$H_m k_m/2$	HiWinGS	3.08E+05	2.40	3.79E-03 – 7.77E-03	0.12	1.63
	SO GasEx	1.55E+02	0.94	3.15E-03 – 6.90E-03	-0.17	1.32
	Combined	1.70E+03	1.36	2.66E-03 – 7.72E-03	-0.05	1.57
$H_p k_p/2$	HiWinGS	5.98E+02	1.27	2.53E-03 – 1.67E-02	0.04	1.60
	SO GasEx	2.28E-01	-0.31	3.63E-03 – 1.21E-02	-0.11	1.30
	Combined	1.23E+02	0.91	2.37E-03 – 1.67E-02	-0.10	1.56

Table 3 – Wave age parameterizations of whitecap coverage (%) determined in this study. Wind-sea only statistics are denoted by a ‘ws’ subscript. Fits and data computed as for Table 1.

Predictor	Experiment	a	n	range	$r^2$	$rmse$
$c_p/U_{10N}$	HiWinGS	2.09E+00	-1.17	0.67 – 2.59	0.08	1.58
	SO GasEx	1.94E+00	-2.11	0.97 – 3.17	0.06	1.24
	Combined	1.96E+00	-1.38	0.67 – 3.64	0.09	1.48
$c_p/u_*$	HiWinGS	1.76E+02	-1.41	14.22 – 80.22	0.24	1.47
	SO GasEx	1.57E+02	-1.41	21.98 – 79.03	-0.04	1.19
	Combined	1.57E+02	-1.38	14.22 – 106.58	0.13	1.39
$c_{p_{ws}}/U_{10N}$	HiWinGS	1.92E+00	-0.54	0.65 – 1.20	-0.11	1.76
	SO GasEx	7.11E-01	-1.04	0.69 – 1.86	-0.11	0.68
	Combined	1.58E+00	-1.02	0.58 – 1.72	-0.08	1.68
$c_{p_{ws}}/u_*$	HiWinGS	2.34E+02	-1.56	13.26 – 30.65	-0.01	1.63
	SO GasEx	6.65E+00	-0.66	16.90 – 49.47	-0.18	0.69
	Combined	2.61E+02	-1.63	12.14 – 47.78	0.04	1.54
$c_m/U_{10N}$	HiWinGS	1.35E+00	-1.40	0.52 – 1.88	0.10	1.61
	SO GasEx	1.31E+00	-3.64	0.81 – 2.27	0.30	0.98
	Combined	1.25E+00	-1.78	0.52 – 2.57	0.16	1.48
$c_m/u_*$	HiWinGS	1.57E+02	-1.51	10.65 – 57.66	0.23	1.51
	SO GasEx	2.82E+03	-2.42	18.55 – 58.00	0.13	1.01
	Combined	2.25E+02	-1.64	10.65 – 77.51	0.22	1.40
$c_{m_{ws}}/U_{10N}$	HiWinGS	1.77E+00	-0.52	0.48 – 0.95	-0.13	1.75
	SO GasEx	5.38E-01	-2.27	0.66 – 1.64	0.00	0.64
	Combined	1.08E+00	-1.42	0.41 – 1.51	0.00	1.64
$c_{m_{ws}}/u_*$	HiWinGS	1.26E+02	-1.48	9.82 – 24.07	0.02	1.67
	SO GasEx	3.57E+01	-1.22	16.80 – 43.85	-0.10	0.65
	Combined	9.99E+01	-1.44	8.11 – 40.25	0.12	1.54

Table 4 – Wave-wind Reynolds number parameterizations of whitecap coverage (%) determined in this study. Wind-sea only statistics are denoted by a ‘ws’ subscript. Fits and data computed as for Table 1.

Predictor	Experiment	$a$	$n$	range	$r^2$	$rmse$
$u_* H_s / \nu_w$	HiWinGS	5.38E-06	0.88	1.95E+05–4.90E+06	0.35	1.39
	SO GasEx	3.16E-08	1.29	3.12E+05–1.59E+06	0.10	1.10
	Combined	3.21E-05	0.76	1.46E+05–6.00E+06	0.25	1.31
$u_* H_{s_{ws}} / \nu_w$	HiWinGS	2.75E-04	0.62	2.40E+05–6.73E+06	0.34	1.45
	SO GasEx	5.98E-05	0.72	2.44E+05–7.24E+05	-0.06	0.71
	Combined	9.91E-05	0.69	1.25E+05–4.29E+06	0.35	1.34
$u_* H_p / \nu_w$	HiWinGS	1.64E-05	0.82	1.45E+05–3.85E+06	0.33	1.41
	SO GasEx	8.83E-08	1.24	2.39E+05–1.22E+06	0.09	1.09
	Combined	5.65E-05	0.74	1.11E+05–4.69E+06	0.24	1.33
$u_* H_{p_{ws}} / \nu_w$	HiWinGS	3.77E-04	0.61	1.90E+05–5.19E+06	0.33	1.46
	SO GasEx	1.93E-07	1.18	2.18E+05–5.88E+05	-0.08	0.73
	Combined	7.03E-05	0.73	1.09E+05–3.43E+06	0.34	1.36
$u_* H_m / \nu_w$	HiWinGS	1.20E-05	0.91	5.50E+04–1.30E+06	0.36	1.42
	SO GasEx	2.10E-07	1.25	1.05E+05–5.25E+05	0.09	1.16
	Combined	5.80E-05	0.79	4.57E+04–1.59E+06	0.24	1.33
$u_* H_{m_{ws}} / \nu_w$	HiWinGS	4.64E-04	0.64	6.06E+04–1.70E+06	0.34	1.45
	SO GasEx	1.13E-04	0.75	5.22E+04–2.30E+05	0.04	0.74
	Combined	2.37E-04	0.70	2.15E+04–1.17E+06	0.35	1.35



1171 *Table 5 – Breaking-wave Reynolds number parameterizations of whitecap coverage (%)*  
1172 *determined in this study. Wind-sea only statistics are denoted by a ‘ws’ subscript. Fits and data*  
1173 *computed as for Table 1.*

Predictor	Experiment	$a$	$n$	range	$r^2$	$1/\text{mse}$
$\frac{u_*^2}{v_w \omega_p}$	HiWinGS	1.85E-04	0.71	2.54E+04 – 1.58E+06	0.42	1.74
	SO GasEx	2.10E-12	2.09	1.66E+05 – 6.60E+05	0.33	0.98
	Combined	1.08E-04	0.74	2.54E+04 – 2.04E+06	0.24	1.34
$\frac{u_*^2}{v_w \omega_{p_{ws}}}$	HiWinGS	2.50E-03	0.52	5.47E+04 – 1.99E+06	0.30	1.44
	SO GasEx	4.10E-06	0.98	1.38E+05 – 3.51E+05	0.00	0.68
	Combined	2.24E-04	0.70	4.70E+04 – 1.31E+06	0.28	1.36
$\frac{u_*^2}{v_w \omega_m}$	HiWinGS	2.39E-04	0.70	1.87E+04 – 1.17E+06	0.40	1.37
	SO GasEx	3.33E-11	1.92	1.40E+05 – 4.77E+05	0.33	0.93
	Combined	1.06E-04	0.76	1.87E+04 – 1.45E+06	0.23	1.32
$\frac{u_*^2}{v_w \omega_{m_{ws}}}$	HiWinGS	1.39E-03	0.58	4.47E+04 – 1.49E+06	0.31	1.42
	SO GasEx	1.93E-06	1.05	1.33E+05 – 2.84E+05	0.06	0.67
	Combined	1.70E-04	0.73	4.15E+04 – 9.62E+05	0.24	1.36

1176 *Table 6 – Result of the linear regression  $\log_{10} W = \log_{10} a + \alpha \log_{10} \left( \frac{c_m}{u_*} \right) + \beta \log_{10} \left( \frac{H_s k_m}{2} \right) +$*   
1177  *$\gamma \log_{10} (H_m u_* / v_w)$*

Experiment		Estimate	T-Stat	pValue
HiWinGS	$a$	1.43E-04	-2.56	1.13E-02
	$\alpha$	-0.77	-3.73	2.62E-04
	$\beta$	-0.03	-0.11	9.14E-01
	$\gamma$	0.86	5.32	3.53E-07
SO GasEx	$a$	7.52E-05	-1.16	2.51E-01
	$\alpha$	-1.33	-2.42	1.85E-02
	$\beta$	-0.66	-1.17	2.47E-01
	$\gamma$	0.82	2.25	2.77E-02
Combined	$a$	1.28E-02	-1.84	6.72E-02
	$\alpha$	-1.01	-5.44	1.40E-07
	$\beta$	0.06	0.29	7.76E-01
	$\gamma$	0.61	5.30	2.77E-07

1178

1179

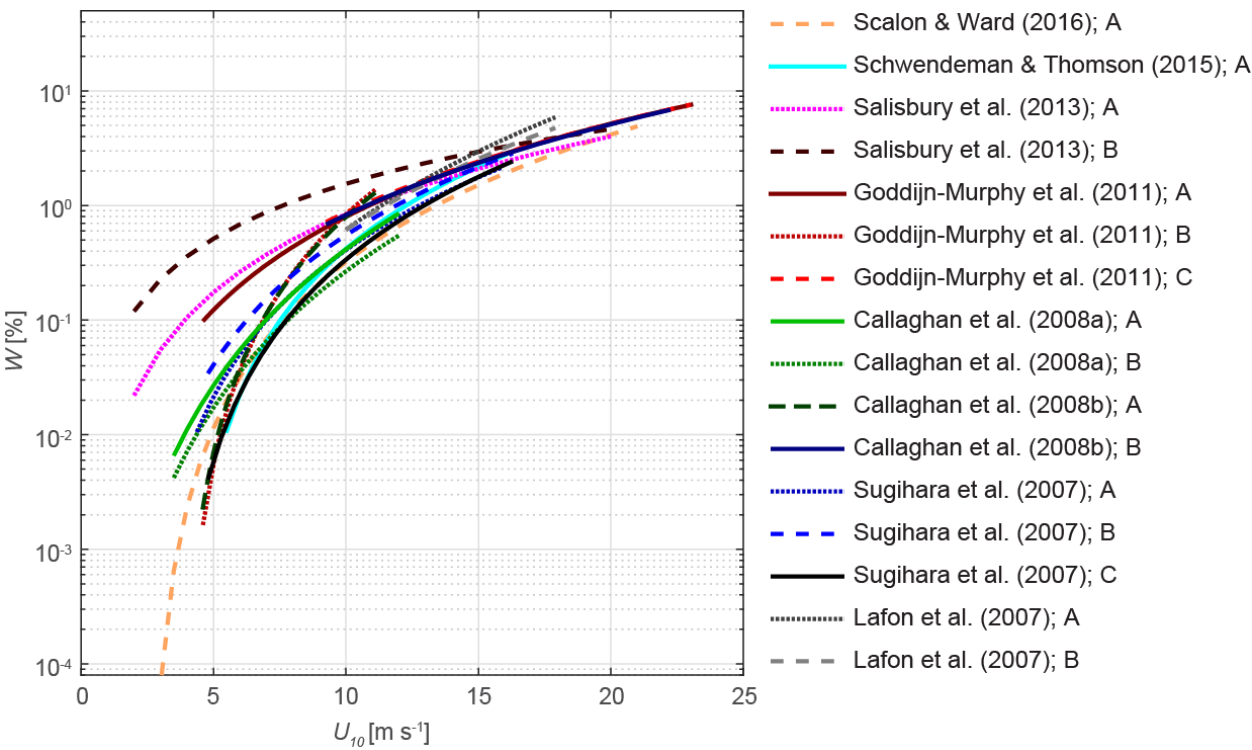


Figure 1 – Parameterizations of Whitecap coverage ( $W$ ) as a function of wind speed ( $U_{10}$ )

published since 2004 (see APPENDIX A).

1180

1181

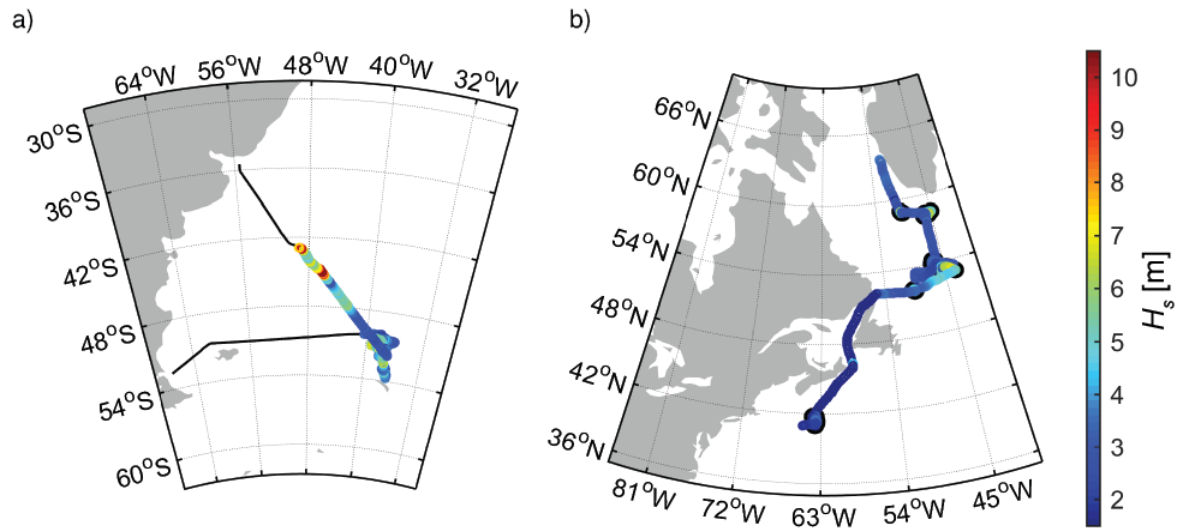


Figure 2 – Ships tracks a) SO GasEx and b) HiWinGS; the color code shows the significant wave height [m]

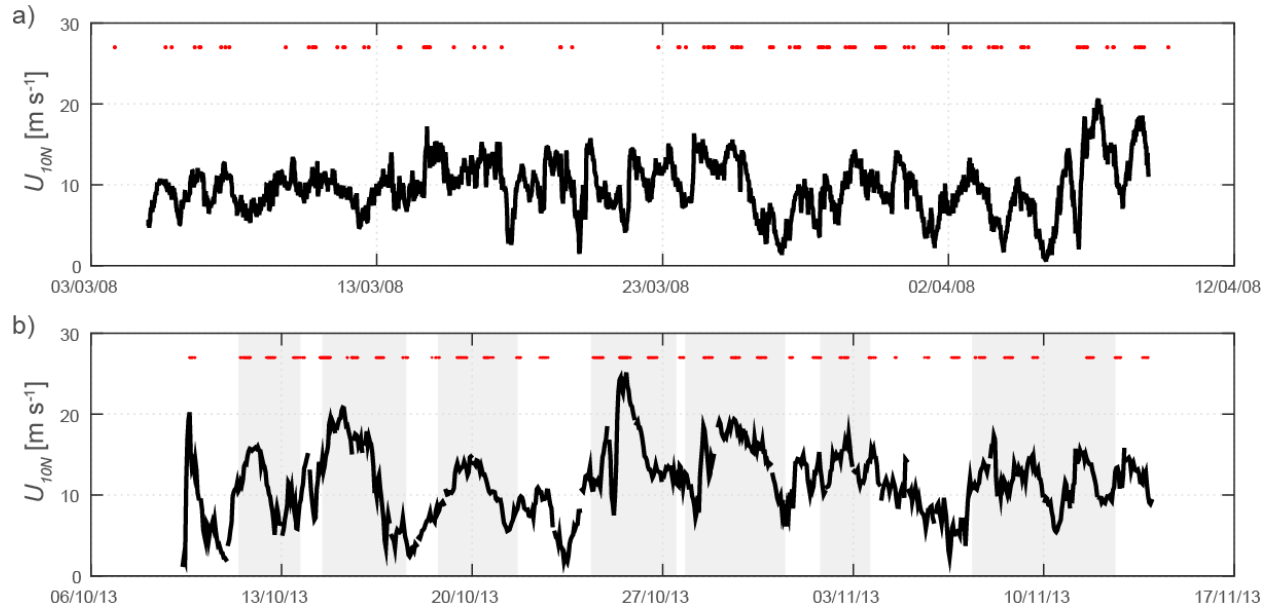
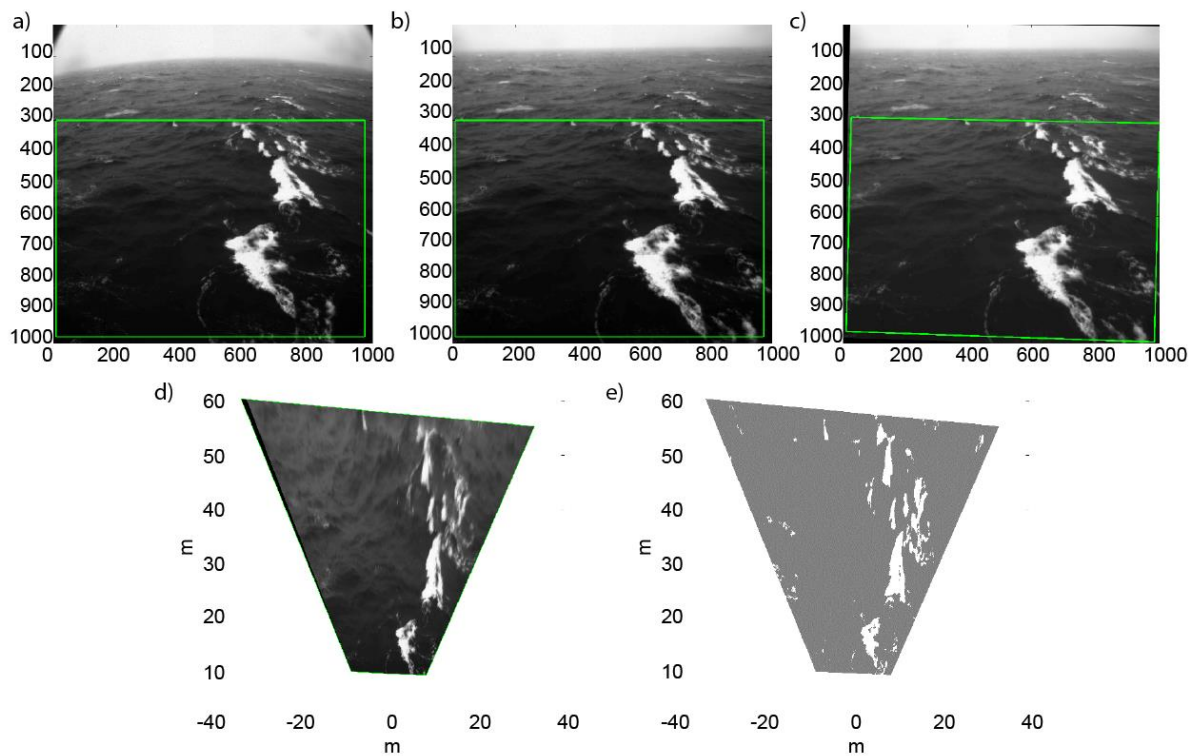


Figure 3 – Wind speed time series; a) for SO GasEx, and b) for HiWinGS. The gray shading represents periods when the ship was on station during HiWinGS. The red lines correspond to periods of visible imagery recording.

1184

1185

1186



*Figure 4 – Steps of the image processing: a) raw image, b) lens calibration, c) roll and yaw correction, d) projection based on incidence angle and height of camera assuming flat surface and e) thresholded and projected image*

1187

1188

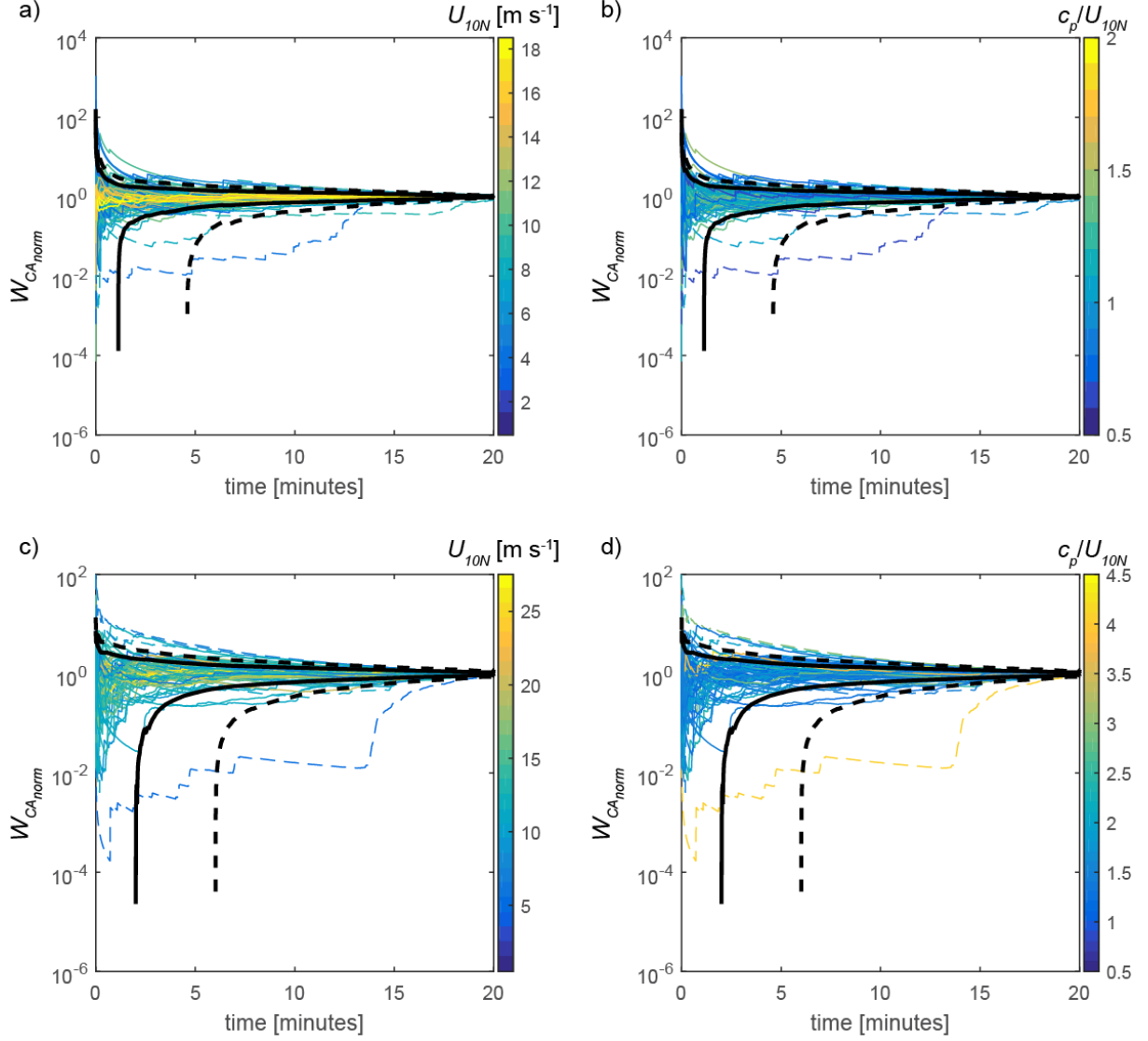


Figure 5 – Time series of the normalized cumulative whitecap coverage  $W_{CA\_norm}$  color-coded by wind speed (a,c) and wave age (b,d) for SO GasEx (a,b) and HiWinGS (c,d). The black solid and dashed lines represent the one and two standard deviations bounds computed from  $W_{CA\_norm}$  of the respective datasets for a given time. Non-converging  $W_{CA\_norm}$  are represented by lines that fall outside of the 2 standard deviations bound after 15 minutes for more than 3 minutes.

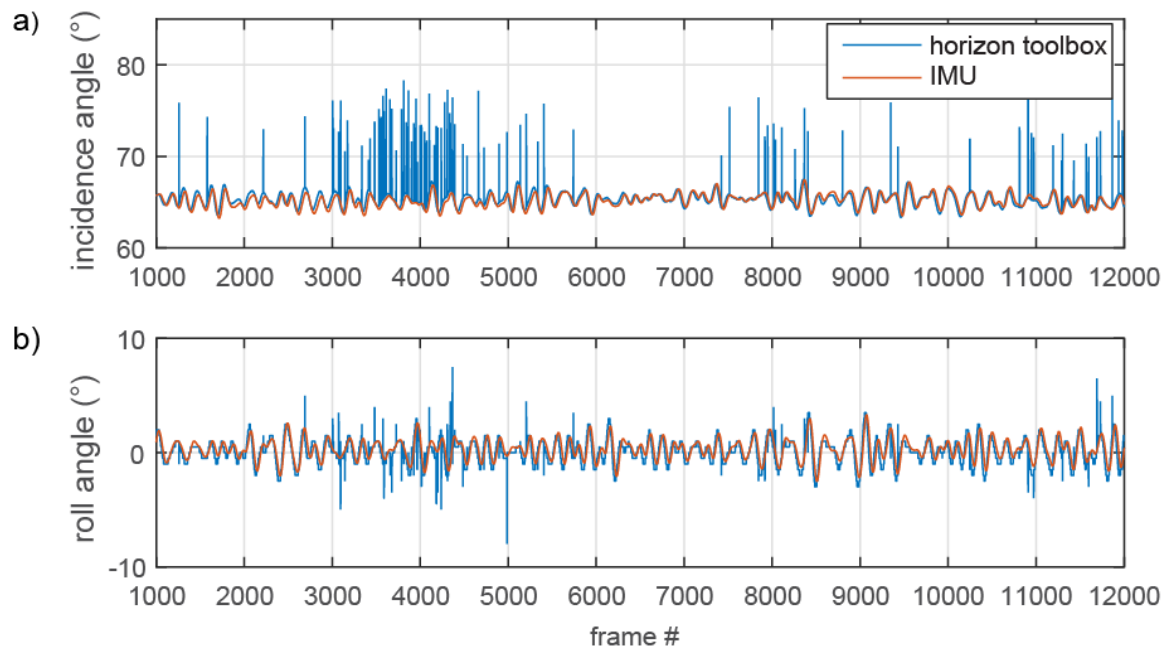


Figure 6 – time series of the a) incidence and b) roll angles measured by the IMU (orange) and determined by the horizon tracking toolbox (blue).

1189

1190



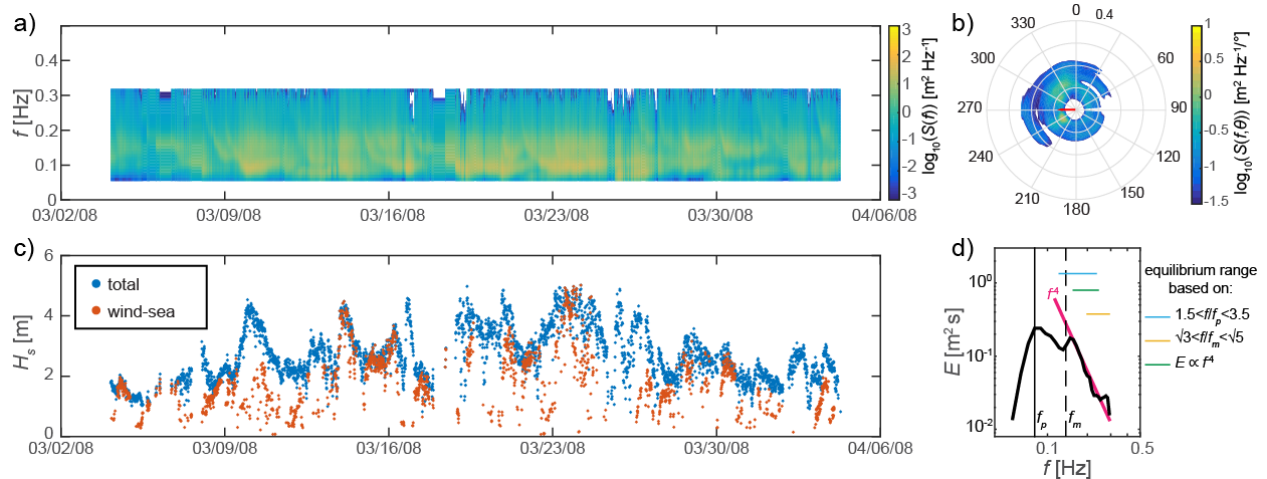


Figure 7 – WAMOS measurements taken during SO GasEx: a) the spectrogram, b) an example of a directional wave spectra, c) the time series of the significant wave height computed from the total spectrum and the wind-sea partition, and d) the omnidirectional wave spectra computed from b) with vertical lines depicting the peak and mean frequencies and horizontal lines showing equilibrium ranges based on the peak frequency, the mean frequency and portion of the spectra proportional to the frequency to the power -4.

1191

1192

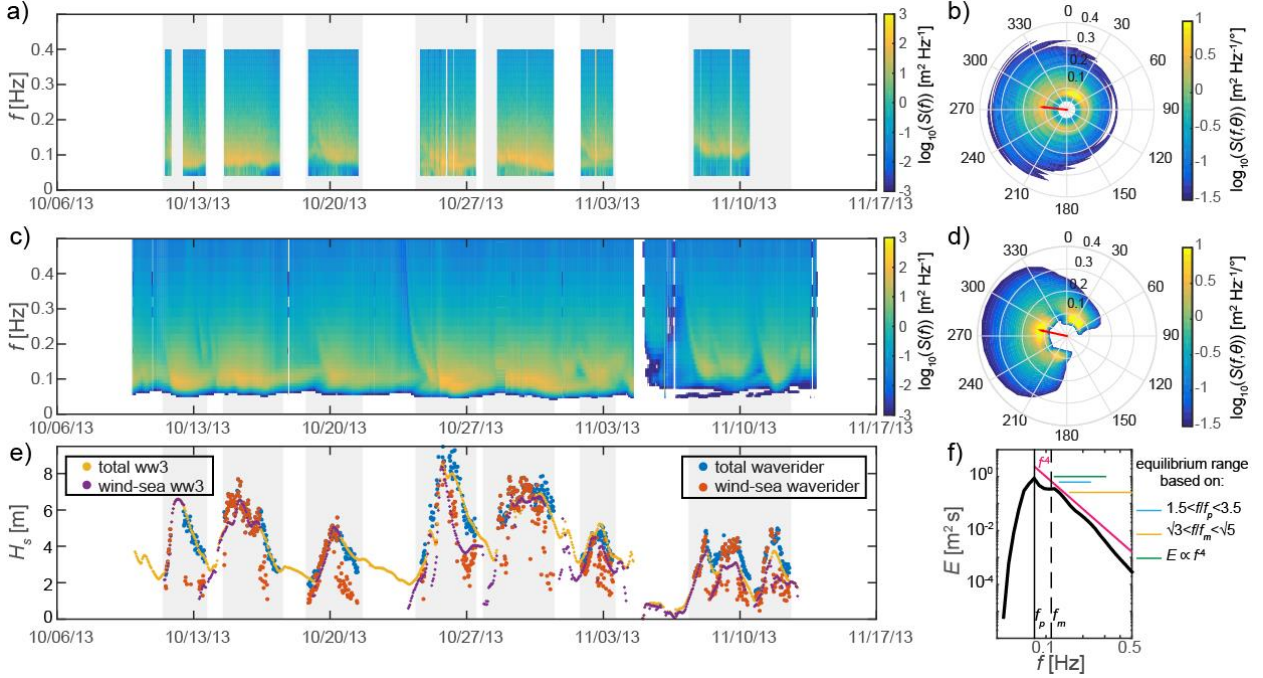


Figure 8– Wave field measurements and model hind cast for HiWinGS. a) and c) show spectragrams from the waverider and from the WAVEWATCH-III® hind cast, respectively. Examples of directional wave spectra from the waverider, and from the WAVEWATCH III® hind cast corresponding to the same time are shown in b) and d). The time series of the significant wave heights computed from the total spectrum and the wind-sea partition of both the waverider and the model hind cast is shown in e), and d) depicts the omnidirectional wave spectra computed from d) with vertical lines depicting the peak and mean frequencies and horizontal lines showing equilibrium ranges based on the peak frequency, the mean frequency and portion of the spectra proportional to the frequency to the power  $-4$ . The grey shading in a), b), and e) indicates periods when the R/V Knorr was on station.

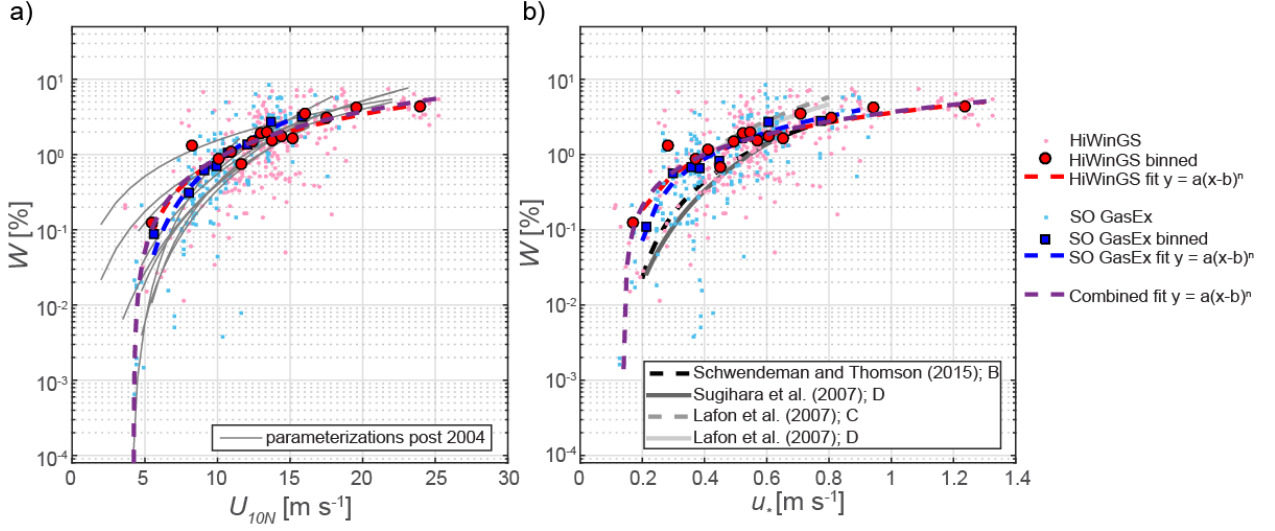


Figure 9 – Whitecap coverage ( $W$ ) as a function of a) the 10 m neutral wind speed ( $U_{10N}$ ) and b) the friction velocity ( $u_*$ ). The small light red dots show the hourly averaged whitecap coverage computed from the HiWinGS dataset, while the small blue squares are the 30 minute averaged whitecap coverage computed from the SO GasEx dataset. The blue squares and red circles show averages of 7 neighboring points for SO GasEx and HiWinGS, respectively. These are used to compute the best fit shown by the dashed red and blue lines. The dark purple lines show the best fits to the binned combined data. The gray lines correspond to the parameterizations summarized in APPENDIX A and APPENDIX D.

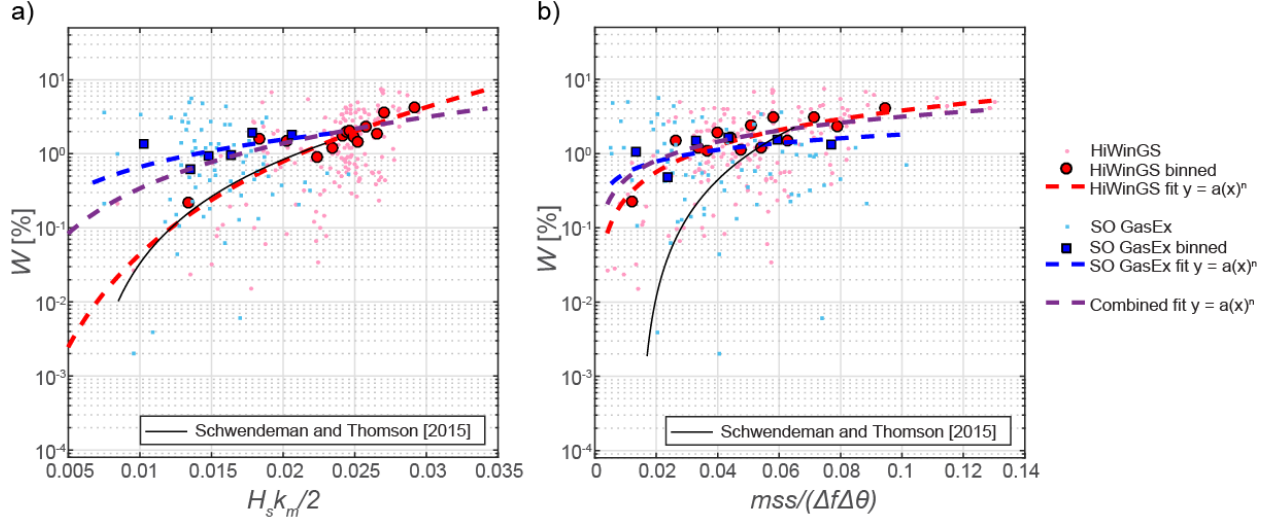


Figure 10 – Whitecap coverage ( $W$ ) as a function of a) mean wave steepness and b) mean square slope normalized by the directional spread and frequency bandwidth. The small light red dots show the hourly averaged whitecap coverage computed from the HiWinGS dataset, while the small blue squares are the 30 minute averaged whitecap coverage computed from the SO GasEx dataset. The blue squares and red circles show averages of 7 neighboring points for SO GasEx and HiWinGS, respectively. These are used to compute the best fit shown by the dashed red and blue lines. The dark purple lines show the best fits to the binned combined data. The black lines correspond to parameterizations of Schwendeman and Thomson (2015b).

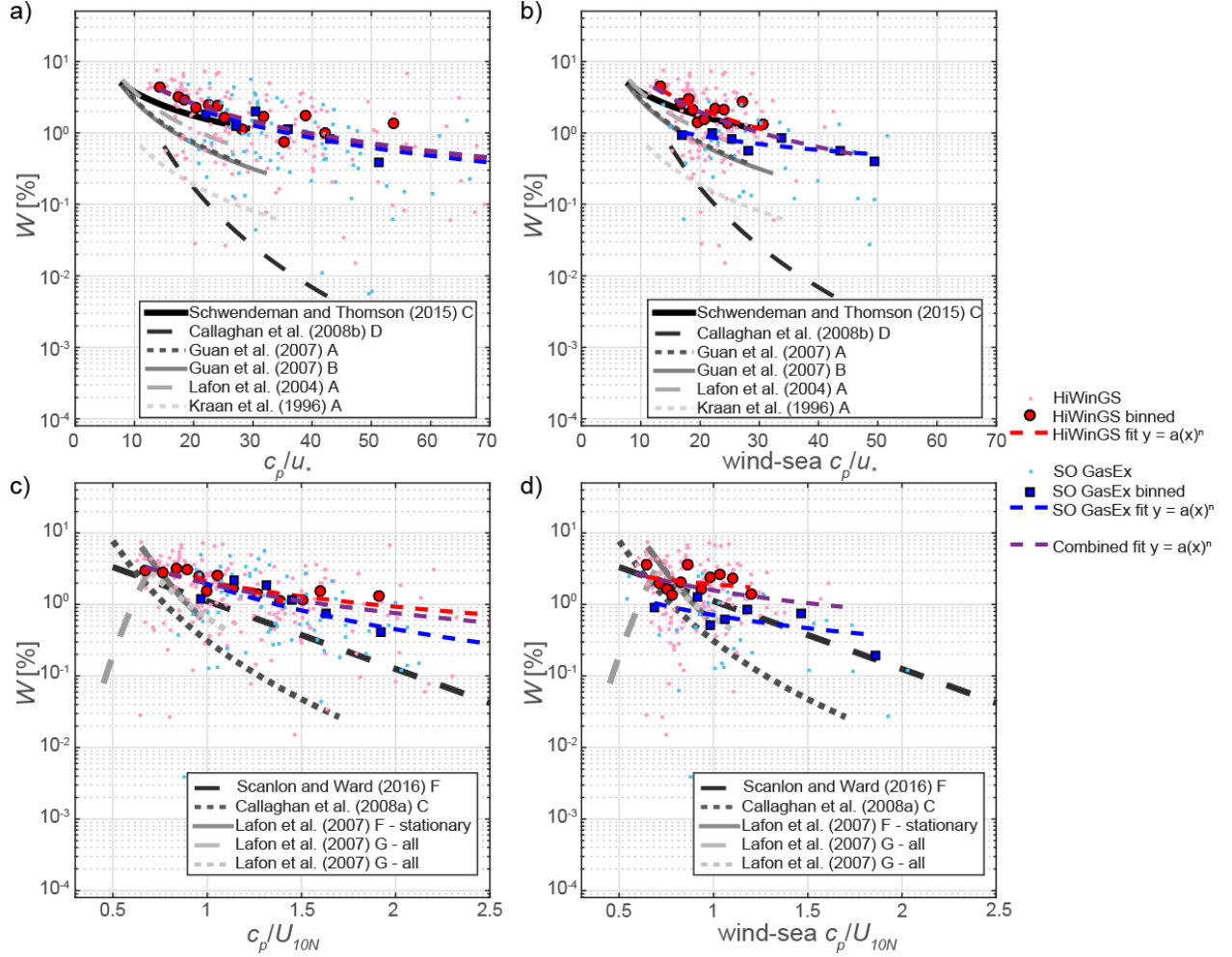


Figure 11 – Whitecap coverage ( $W$ ) as a function of wave age a)  $\frac{c_p}{u_*}$ , b)  $\frac{c_p}{u_*}$  using the wind-sea spectral peak, c)  $c_p/U_{10N}$  using the wind-sea spectral peak, and d)  $c_p/U_{10N}$  .whitecap coverage. The small light red dots show the hourly averaged whitecap coverage computed from the HiWinGS dataset, while the small blue squares are the 30 minute averaged whitecap coverage computed from the SO GasEx dataset. The blue squares and red circles show averages of 7 neighboring points for SO GasEx and HiWinGS, respectively. These are used to compute the best fit shown by the dashed red and blue lines. The dark purple lines shows the best fit to the binned combined data. The black and gray lines correspond to the parameterizations summarized in APPENDIX C.

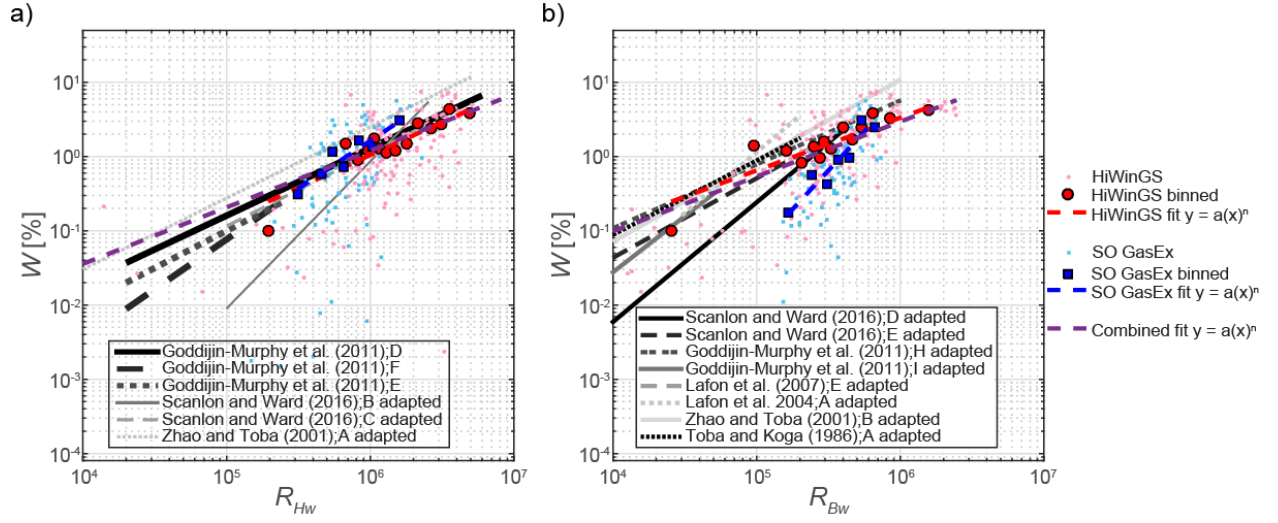


Figure 12 – Whitecap coverage ( $W$ ) as a function of a) wave-wind and b) breaking-wave Reynolds number computed from the significant wave height and peak angular velocity of the entire wave spectrum. The small light red dots show the hourly averaged whitecap coverage computed from the HiWinGS dataset, while the small blue squares are the 30 minute averaged whitecap coverage computed from the SO GasEx dataset. The blue squares and red circles show averages of 7 neighboring points for SO GasEx and HiWinGS, respectively. These are used to compute the best fit shown by the dashed red and blue lines. The dark purple lines shows the best fit to the binned combined data. The black and gray lines correspond to the parameterizations summarized in APPENDIX B.

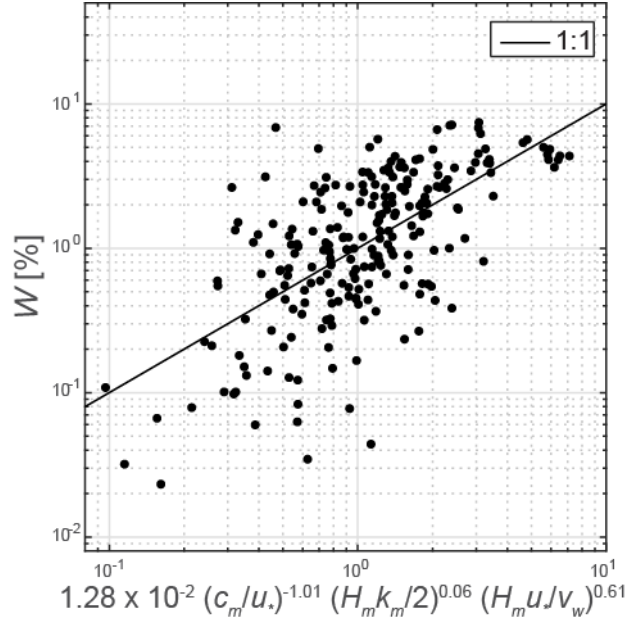


Figure 13- Scatter plot of the measured whitecap coverage [W] plotted against the multiple parameter model:

$$W = a \left( \frac{c_m}{u_*} \right)^\alpha \left( \frac{H_m k_m}{2} \right)^\beta \left( \frac{H_m u_*}{v_w} \right)^\gamma. \text{ In black the 1:1 line.}$$

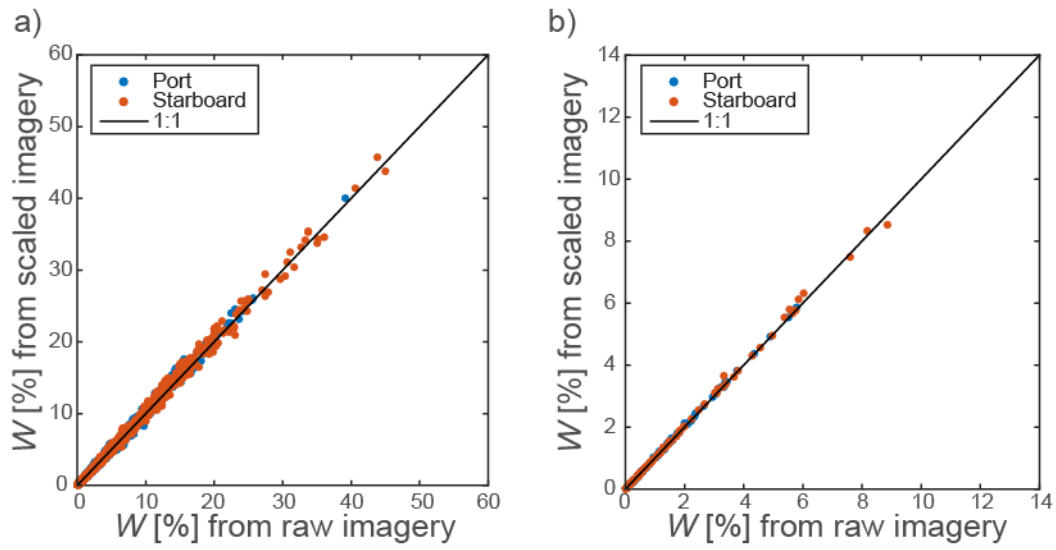


Figure 14- Scatter plots of the whitecap coverage ( $W$ ) estimated from the scaled and non-scales imagery a) individual frames, and b) 20 minute averages

1200

1201